

See discussions, stats, and author profiles for this publication at: <https://www.researchgate.net/publication/272847199>

# Numerical simulation of interactions between free surface and rigid body using a robust SPH method

Article *in* Ocean Engineering · April 2015

Impact Factor: 1.35 · DOI: [10.1016/j.oceaneng.2015.01.019](https://doi.org/10.1016/j.oceaneng.2015.01.019)

---

CITATIONS

4

READS

242

3 authors, including:



Pengnan Sun

Harbin Engineering University

6 PUBLICATIONS 8 CITATIONS

[SEE PROFILE](#)



Furen Ming

Hanoi University of Law

5 PUBLICATIONS 14 CITATIONS

[SEE PROFILE](#)



# Numerical simulation of interactions between free surface and rigid body using a robust SPH method



Pengnan Sun, Furen Ming, Aman Zhang\*

College of Shipbuilding Engineering, Harbin Engineering University, Harbin 150001, China

## ARTICLE INFO

### Article history:

Received 14 April 2014

Accepted 31 January 2015

### Keywords:

SPH

Free surface flow

Fluid–solid interaction

Dummy particle boundary

Free-slip

No-slip

## ABSTRACT

A robust weakly compressible SPH method is applied to simulate violent interactions between free surface and rigid body. Artificial density and viscosity diffusion are applied to stabilize the pressure field. The calculation of forces and torques on rigid body is improved for higher accuracy. Improved dummy particle technique for stationary and moving boundary is analyzed and applied in both free-slip and no-slip condition. For the velocity divergence approximation near the dummy particle boundary, it is proved that substituting the velocity of the rigid body directly into the divergence operator is acceptable and reasonable. For the viscous stress calculation, the dummy particle velocity extension manners in both free-slip and no-slip boundary condition are given in higher accuracy. The present solid boundary technique is convenient for both two-dimensional (2-D) and three-dimensional (3-D) models. Stability and accuracy of the present SPH scheme are tested by four 2-D cases and two 3-D cases, and the results agree well with both experimental data and other numerical results. The present SPH scheme is potential for some ocean engineering applications with violent fluid–solid interactions.

© 2015 Elsevier Ltd. All rights reserved.

## 1. Introduction

The interactions between free surface and rigid body are very important in ocean engineering. The phenomena include the coupling motions between floating structures and water waves ([Faltinsen, 1993](#)), various shapes of objects (jackets, lifeboats, seaplanes, and so on) dropping onto water surface ([Sun and Faltinsen, 2006](#)), green water loading on the deck equipment ([Buchner, 2002](#)), water waves striking on the ship side ([Lighthill, 1986](#)), sloshing in LNG ships or oil tanks ([Faltinsen and Timokha, 2009](#)) and so on. These violent fluid–solid interactions have been increasingly concerned by fluid dynamicists since they may make the floating body substantially heaving, rolling and cause great pressure loading on local parts of the structures and even damage them ([Faltinsen, 1993](#)). In ocean engineering realm, such phenomena are always accompanied with large deformation of free surface, splashing and fragmentation of water waves ([Bouscasse et al., 2013](#)), which make traditional method encounter a lot of difficulties.

When the dimension of the structure is not extremely large, the structure is usually considered as a rigid body. While studying those structures with enormous scale, like aircraft carriers or large container ships, effects of water elasticity need to be considered, which is beyond the scope of this paper. At present, studies on the interactions between free surface and rigid body have made great progress, which can be mainly classified into two groups: the theoretical prediction and the experimental research. Due to the complexity and strong nonlinearity of real flows in the nature, the experimental results are more reliable for the engineering design. However, there are some unique problems existing in experimental researches ([Newman, 1977](#)), such as the scale effects which make the experimental phenomena not able to reflect the real engineering conditions. Therefore, the technology of Numerical Water Tanks (NWTs) has been developing rapidly ([Wang et al., 1995](#)). Up to now, based on the potential flow theory by introducing some assumptions (incompressible, irrotational, non-viscous, etc.), some theoretical solutions about water waves ([Newman, 1977](#)), fluid–solid interactions ([Sun and Wu, 2013](#)) have been found. However, these theoretical solutions are only limited to extremely ideal cases, while the conditions are quite complex in ocean engineering practice, so various numerical methods are developed. The widely used numerical methods in ocean engineering are mostly based on potential flow theory, like Mixed Eulerian–Lagrangian Boundary Element Method (BEM–MEL) ([Faltinsen, 1977](#)). However, when the free surface is broken, the

\* Correspondence to: College of Shipbuilding Engineering, Harbin Engineering University, Room 513, Chuanhai Building, No. 145 Nantong Street, Nangang District, Harbin 150001, China. Tel.: +86 451 82518443; fax: +86 451 82518296.

E-mail addresses: [sunpengnan@yeah.net](mailto:sunpengnan@yeah.net) (P. Sun), [mingfuren@gmail.com](mailto:mingfuren@gmail.com) (F. Ming), [zhangaman@hrbeu.edu.cn](mailto:zhangaman@hrbeu.edu.cn) (A. Zhang).

calculations become hard to continue. Therefore, a robust numerical method is needed, which should be able to simulate those fluid–solid interactions in time domain with few limitations.

With the rapid development of computational technology, the Computational Fluid Dynamics (CFD) has been widely applied in the field of ocean engineering. CFD can be classified into two groups: grid methods and meshless methods. Grid methods include Finite Element Method (FEM) ([Wu et al., 1998](#)), Finite Different Method (FDM) ([Chung, 2010](#)), Finite Volume Method (FVM) ([Kleefsman et al., 2005](#)), etc. Due to the existence of free surface and its large deformation in ocean engineering, the complexity and difficulty of Euler grid methods (e.g. VOF, Level Set, etc.) increase a lot for the free surface tracking. Even for the Lagrangian grid method, such as FEM, too large grid deformations may lead to calculation errors or collapses. The Lagrangian characteristics of meshless methods make them easy in modeling free surface flows, especially for water wave splashing and fragmentation. Recently, Smoothed Particle Hydrodynamics (SPH) method ([Colagrossi and Landrini, 2003](#)) and Moving Particle Semi-implicit (MPS) method ([Khayyer and Gotoh, 2012; Koshizuka and Oka, 1996](#)) have been developing rapidly and used to simulate free surface flows. A robust SPH framework is applied in this paper to simulate violent fluid–solid interactions.

SPH method was originally proposed to simulate astrodynamics which is boundless ([Gingold and Monaghan, 1977](#)), and then it was used to simulate incompressible free surface flows by [Monaghan \(1994\)](#). Up to now, SPH has been tested with variable cases ([Liu and Liu, 2010](#)), including dam breaking ([Marrone et al., 2011](#)), tsunami ([St-Germain et al., 2012](#)), sloshing ([Landrini et al., 2003; Zheng et al., 2012](#)), multiphase flow ([Grenier et al., 2009](#)), etc. For the SPH algorithm, two most enormous challenges are the boundary implementation and the pressure calculation. Due to the lacking of fluid particles outside the boundary (both the free surface boundary and the solid wall boundary), the SPH approximation adjacent to the boundary will be less accurate. It is proved in [Colagrossi et al. \(2009\)](#) that the free surface condition can be satisfied implicitly in SPH framework. Therefore, literatures pay more attention to the solid wall boundary ([Liu et al., 2012](#)). Various solid wall boundary methods have been introduced, including the repulsive force boundary ([Monaghan and Kajtar, 2009](#)), the normal flux method ([De Leffe et al., 2009](#)), the mirroring ghost boundary ([Colagrossi and Landrini, 2003](#)), the fixed ghost boundary ([Marrone et al., 2011](#)), the coupled dynamic SBT algorithm ([Liu et al., 2012](#)), the dummy particle boundary ([Adami et al., 2012](#)) and so on. The interpolation area would be cut off by boundary line in the repulsive force boundary, so the inconsistency may exists, while it can model arbitrary shapes of boundary in both 2-D and 3-D cases. In normal flux method, the kernel truncation due to the lacking of particles outside the boundary is calculated through a surface integral on the solid boundary surface, and this method can also be implemented in both 2-D and 3-D cases ([Marrone, 2012](#)). The mirroring ghost boundary has been proved to be inconsistent in the pressure gradient approximation near the boundary ([Merino-Alonso et al., 2013](#)), and it is also hardly to be used in curved solid boundary, so it is not suitable for engineering applications. The fixed ghost boundary is an improvement to the mirroring ghost boundary, but it is hard to be implemented in 3-D cases ([Marrone, 2012](#)). In this paper, numerical and theoretical analyses of the dummy particle boundary are presented and first-order accuracy is achieved which implies that the solutions will converge to accurate results as the particle resolution increases. The modeling and implementation of the dummy particle boundary in both 2-D and 3-D cases are easy, and therefore it is adopted in this paper to simulate some violent fluid–solid interaction cases.

According to the current published literatures, SPH algorithms can be classified into two groups: Incompressible Smoothed Particle Hydrodynamics (ISPH) and Weakly Compressible Smoothed Particle Hydrodynamics (WCSPH). Some literatures compared these two

methods with some test cases ([Lee et al., 2008, 2010](#)). It is concluded that the time step of ISPH is obviously larger than WCSPH, and the pressure field of ISPH is with less pressure noises. So ISPH seems better than WCSPH in the applications of ocean engineering. However, WCSPH has its own advantages for the simpler programming and parallelized computing which will dramatically reduce the time of computation and allow for significantly higher particle resolution ([Molteni and Colagrossi, 2009](#)). As for the pressure noise in WCSPH, two approaches have been introduced in literatures: MLS density filter ([Colagrossi and Landrini, 2003](#)) and adding dissipation terms ([Molteni and Colagrossi, 2009](#)). It is proved in [Sibilla \(2007\)](#) that, for a long time simulating, the MLS filtering can cause significant non-conservation of the total volume in the flow field. Since the dissipation terms added in the continuity equation and the momentum equation are conservative ([Antuono et al., 2012](#)), they are used in the present work, and the pressure noise in the flow field is reduced, see in [Section 3](#).

Recently, fluid–solid interaction cases such as solid body entering calm water were simulated in ISPH framework with reduced temporal noises ([Skillen et al., 2013](#)). Earlier, similar fluid–solid interaction cases were simulated with WCSPH ([Gong et al., 2009, 2010; Oger et al., 2006; Vandamme et al., 2011; Zhang et al., 2013](#)). However, it is essential to improve the boundary treatment in WCSPH to achieve more reliable results. Besides, the implementation should be convenient enough for the practical engineering applications. The present SPH scheme with the dummy particle boundary is qualified to model complex boundary shapes easily in both 2-D and 3-D cases. Besides, the SPH system in the present work is more accurate and stable with the improved Gaussian kernel ([Grenier et al., 2009](#)). Moreover, by adding dissipation terms ([Antuono et al., 2012](#)) into the discretized equations, the scheme in the present work can approximate the dynamic pressure on the surface of stationary or moving solid body accurately and the results agree well with both experimental data and other numerical results.

The paper is organized as follows: In [Section 2](#), basic principle of SPH is briefly introduced, and then detailed descriptions about the present SPH framework including discretized equations, improved boundary implementation and method of time stepping are presented. [Section 3](#) consists of four 2-D cases and two 3-D cases. A lid-driven cavity test case is adopted first to test the accuracy and stability of the viscous model. Then a rigid box rotating and sinking in viscous fluid is simulated and the results are validated by other numerical results. Afterwards, water entry of cylinder and water entry of wedge are tested, respectively. Compared with either experimental data or other numerical results, good agreements are achieved in the results of the present SPH method. In 3-D cases, a classic 3-D dam breaking test is simulated first, then 3-D cylinder water entry case is performed and the results of SPH are verified by our own experimental data. It is demonstrated that the present SPH framework is good at modeling both 2-D and 3-D interactions between free surface and rigid body.

## 2. The present model

### 2.1. Basic principle of SPH

#### 2.1.1. Kernel approximation

A generic quantity  $f(\mathbf{x})$  at a certain material position  $\mathbf{x}$  can be interpolated with kernel approximation over the compactly supported domain  $\Omega$  ([Liu and Liu, 2003](#)),

$$f(\mathbf{x}) \approx \langle f(\mathbf{x}) \rangle = \int_{\Omega} f(\mathbf{x}') W(\mathbf{x} - \mathbf{x}', h) d\mathbf{x}' \quad (1)$$

where  $\langle f(\mathbf{x}) \rangle$  is the kernel approximation of  $f(\mathbf{x})$ .  $\mathbf{x}'$  denotes the material positions in the compactly supported domain.  $W(\mathbf{x} - \mathbf{x}', h)$  is a kernel function, which has the following properties:

$$\begin{aligned} \int_{\Omega} W(\mathbf{x} - \mathbf{x}', h) d\mathbf{x}' &= 1 \\ \lim_{h \rightarrow 0} W(\mathbf{x} - \mathbf{x}', h) &= \delta(\mathbf{x} - \mathbf{x}') \\ W(\mathbf{x} - \mathbf{x}', h) &= 0, \quad |\mathbf{x} - \mathbf{x}'| > \kappa h \\ \int_{\Omega} \nabla W(\mathbf{x} - \mathbf{x}', h) d\mathbf{x}' &= 0 \end{aligned} \quad (2)$$

where  $h$  is the smoothing length.  $\kappa h$  is the radius of the compactly supported domain  $\Omega$ .  $W(\mathbf{x} - \mathbf{x}', h)$  is an even function about  $\mathbf{x}$ , which makes the kernel approximation satisfy second order accuracy, for more details, see in Liu and Liu (2003).

Similar to Eq. (1), the gradient of  $f(\mathbf{x})$  can be interpolated by kernel approximation in its supported domain:

$$\nabla_{\mathbf{x}} f(\mathbf{x}) \approx \langle \nabla_{\mathbf{x}} f(\mathbf{x}) \rangle = \int_{\Omega} \nabla_{\mathbf{x}} f(\mathbf{x}') W(\mathbf{x} - \mathbf{x}', h) d\mathbf{x}' \quad (3)$$

where  $\nabla_{\mathbf{x}}$  denotes the gradient versus  $\mathbf{x}$ . With integration by parts and using the divergence theorem, Eq. (3) can be rewritten as

$$\nabla_{\mathbf{x}} f(\mathbf{x}) \approx \int_{\partial\Omega} f(\mathbf{x}') W(\mathbf{x} - \mathbf{x}', h) \mathbf{n} dS - \int_{\Omega} f(\mathbf{x}') \nabla_{\mathbf{x}} W(\mathbf{x} - \mathbf{x}', h) d\mathbf{x}' \quad (4)$$

where  $\mathbf{n}$  is the unit normal on the integral boundary  $\partial\Omega$ . In Eq. (4), for the compactly supported property of  $W(\mathbf{x} - \mathbf{x}', h)$ , see in Eq. (2), the first term on the right-hand side of Eq. (4) is null if there is no kernel truncation. Note that, in the simulation of free surface flows, even though the kernel is truncated on the free surface, considering the first term on the right-hand side of Eq. (4) to be null is still acceptable if the value of  $f(\mathbf{x}')$  is zero on the free surface, for more details, see in Colagrossi et al. (2009). Due to the symmetric property, the derivative of  $W(\mathbf{x} - \mathbf{x}', h)$  has the following property:

$$\nabla_{\mathbf{x}} W(\mathbf{x} - \mathbf{x}', h) = -\nabla_{\mathbf{x}'} W(\mathbf{x} - \mathbf{x}', h) \quad (5)$$

Then, Eq. (4) is reduced as

$$\nabla_{\mathbf{x}} f(\mathbf{x}) \approx \int_{\Omega} f(\mathbf{x}') \nabla_{\mathbf{x}} W(\mathbf{x} - \mathbf{x}', h) d\mathbf{x}' \quad (6)$$

The approximation of  $\nabla_{\mathbf{x}} \cdot f(\mathbf{x})$  is similar to  $\nabla_{\mathbf{x}} f(\mathbf{x})$ . The final kernel approximation equation is as follows:

$$\nabla_{\mathbf{x}} \cdot f(\mathbf{x}) \approx \langle \nabla_{\mathbf{x}} \cdot f(\mathbf{x}) \rangle = \int_{\Omega} f(\mathbf{x}') \cdot \nabla_{\mathbf{x}} W(\mathbf{x} - \mathbf{x}', h) d\mathbf{x}' \quad (7)$$

### 2.1.2. Particle approximation

In SPH method, the solution domain is usually discretized into uniformly distributed particles. The particles carry the field variables like pressure, density, velocity, acceleration and other concerned physical quantities, and they are moved by pressure gradient and viscous stress in the flow field. The continuous integration can be approximated with the sum of finite particle volumes in the compactly supported domain. The above process is named as particle approximation (Liu and Liu, 2003). Therefore, the basic SPH equations can be obtained as follows:

$$\left\{ \begin{array}{l} f(\mathbf{x}_i) = \sum_j f(\mathbf{x}_j) W(\mathbf{x}_i - \mathbf{x}_j, h) V_j \\ \nabla_i f(\mathbf{x}_i) = \sum_j f(\mathbf{x}_j) \nabla_i W(\mathbf{x}_i - \mathbf{x}_j, h) V_j \\ \nabla_i \cdot f(\mathbf{x}_i) = \sum_j f(\mathbf{x}_j) \cdot \nabla_i W(\mathbf{x}_i - \mathbf{x}_j, h) V_j \end{array} \right. \quad (8)$$

where the subscript  $i$  denotes the concerned particle,  $j$  denotes the particle within the compactly supported domain of particle  $i$ .  $V_j$  denotes the volume of particle  $j$ .  $V_j$  can be calculated by  $m_j/\rho_j$ , where  $m$  and  $\rho$  denote mass and density, respectively.

The selection of kernel function directly affects the computational efficiency, accuracy and stability of SPH simulations. A comparative study of more than 10 kinds of kernel functions is made in Hongbin and Xin (2005). The conclusion is obtained that the 5th spline kernel function and the Gaussian kernel function are optimal in terms of accuracy and stability. Thus in the present work, an improved Gaussian kernel function (Grenier et al., 2009) is applied:

$$W(\mathbf{x}_i - \mathbf{x}_j, h) = \begin{cases} \alpha_d \left[ \frac{e^{-(r/h)^2} - c_0}{1 - c_1} \right] & \text{if } r \leq 3h \\ 0 & \text{otherwise} \end{cases} \quad c_0 = e^{-9}; \quad c_1 = 10c_0 \quad (9)$$

where  $r = |\mathbf{x}_i - \mathbf{x}_j|$  denotes the distance between the concerned particle  $i$  and the adjacent particle  $j$ . According to the analysis in Dehnen and Aly (2012), the increase of the number  $N_H$  of neighbor particles may produce pairing (or clumping) instability. In the present work, considering both accuracy and stability,  $h = 1.23\Delta x$  is adopted where  $\Delta x$  denotes the initial particle spacing in Cartesian coordinate system, and therefore in the numerical scheme,  $N_H \approx 45$  in 2-D problems and  $N_H \approx 200$  in 3-D problems.  $\alpha_d$  is set to be  $1/(\pi^{1/2}h)$ ,  $1/(\pi h^2)$ ,  $1/(\pi^{3/2}h^3)$  for 1-D to 3-D problems, respectively. In the following part of this article,  $W(\mathbf{x}_i - \mathbf{x}_j, h)$  is noted as  $W_{ij}$ .

### 2.2. Governing equations and their discretized forms

The mass and momentum conservation equations based on the views of Lagrange are as follows:

$$\frac{D\rho}{Dt} = -\rho \nabla \cdot \mathbf{u} \quad (10)$$

$$\rho \frac{D\mathbf{u}}{Dt} = -\nabla p + \mathbf{F}_V + \mathbf{F}_B \quad (11)$$

where  $\mathbf{u}, p, \mathbf{F}_V, \mathbf{F}_B$  denote velocity, pressure, viscous stress and body force, respectively. In the present work, the viscosity of the fluid is approximated by an artificial viscous term, and the body force  $\mathbf{F}_B$  here is the gravity  $\rho g$ .

Eqs. (10) and (11) are non-closed, and it is a common practice in WCSPH to establish the relationship between pressure  $p$  and density  $\rho$  with an equation of state (Monaghan, 1994):

$$p = \frac{c_0^2 \rho_0}{7} \left[ \left( \frac{\rho}{\rho_0} \right)^7 - 1 \right] \quad (12)$$

The equation of state above is the most widely used form in SPH literatures. Furthermore, its linear form has been proved to be more stable and with less pressure noises (Antuono et al., 2012). Thus it is adopted here:

$$p = c_0^2 (\rho - \rho_0) \quad (13)$$

where  $\rho_0$  is the reference density at null pressure,  $c_0$  is an artificial sound speed which depends on the maximum velocity in the flow in order to keep the variation of particle density within 1% (Monaghan, 1994). When ignoring viscous stress and surface tension, the artificial sound speed  $c_0$  can be determined by

$$\left( \frac{\max(\mathbf{u}^2)}{c_0^2}, \frac{gH}{c_0^2} \right) < 0.01 \quad (14)$$

In the discretized SPH formulations, artificial density diffusion in Molteni and Colagrossi (2009) is added to the continuity equation in this work, through which the pressure noise is reduced. In order to make the calculation accurate and stable, artificial viscosity term of Monaghan and Gingold (1983) is added into the momentum equation. This term can make the particles distribute uniformly in the flow field. Besides, both linear and angular momentum conservation is achieved because the forces are all in the center directions of the particle pairs. Note that the

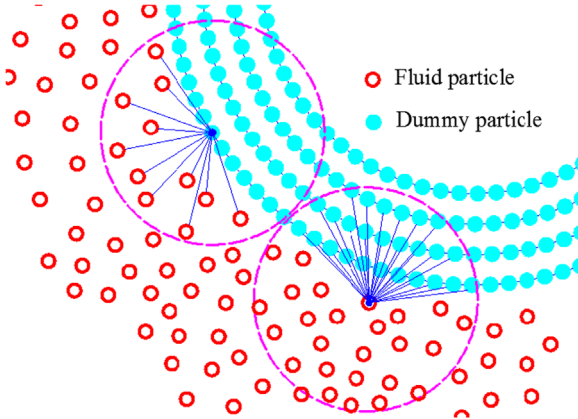


**Fig. 1.** Sketch of the dummy particle boundary in two dimensional. (For interpretation of the references to color in this figure legend, the reader is referred to the web version of this article.)

discretized form of momentum equation in the present SPH system is similar to [Hu and Adams \(2007\)](#), in which a density-weighted inter-particle averaged pressure  $\tilde{p}_{ij}$  is used. Since the discretized formulation with the use of both  $V_i$  and  $V_j$  can ensure the continuity of  $(\nabla p/\rho)_{ij}$  between particle  $i$  and particle  $j$ , it is used here. The present SPH system is as follows:

$$\frac{D\rho_i}{Dt} = \rho_i \sum_j (\mathbf{u}_i - \mathbf{u}_j) \cdot \nabla_i W_{ij} V_j + \delta h c_0 \sum_j \psi_{ij} \nabla_i W_{ij} V_j \quad (15)$$

$$\frac{D\mathbf{u}_i}{Dt} = -\frac{1}{m_i} \sum_j (V_i^2 + V_j^2) \tilde{p}_{ij} \nabla_i W_{ij} + \mathbf{g} + \alpha h c_0 \frac{\rho_0}{\rho_i} \sum_j \pi_{ij} \nabla_i W_{ij} V_j \quad (16)$$

$$\frac{D\mathbf{x}_i}{Dt} = \mathbf{u}_i \quad (17)$$

$$\rho_i = c_0^2 (\rho_i - \rho_0) \quad (18)$$

$$\psi_{ij} = \frac{(\rho_i - \rho_j)(\mathbf{r}_i - \mathbf{r}_j)}{|\mathbf{r}_i - \mathbf{r}_j|^2 + (0.01h)^2}, \quad \tilde{p}_{ij} = \frac{\rho_j p_i + \rho_i p_j}{\rho_i + \rho_j}, \quad \pi_{ij} = \frac{(\mathbf{u}_i - \mathbf{u}_j) \cdot (\mathbf{r}_i - \mathbf{r}_j)}{|\mathbf{r}_i - \mathbf{r}_j|^2 + (0.01h)^2} \quad (19)$$

Generally, parameter  $\delta$  is set to be 0.2 and the pressure field is stable ([Antuono et al., 2010](#)). The relation between the parameter  $\alpha$  in Eq. (16) and the kinematic viscosity  $\nu$  of the fluid has been addressed in [Monaghan \(2005\)](#) that

$$\alpha = \frac{2(d+2)}{h c_0} \quad (20)$$

where  $d$  is the dimension of the problem. In general ocean engineering practice, the scale of floating structure is so large that the Reynolds number is high. The viscous effect can be ignored, and therefore free-slip boundary condition is usually implemented. The artificial viscous force is only calculated for fluid particles when free-slip boundary is implemented ([Adami et al., 2012](#)). In these cases, the parameter  $\alpha$  is usually chosen for keeping a so-called local Reynolds number  $Re_h = Uh/\nu$  no larger than  $O(10)$  in order to ensure the simulation stable and accurate ([Bouscasse et al., 2013](#)). In the present work, the parameter  $\alpha$  is set to be 0.1 if real viscosity of the fluid is not mentioned.

While for the fluid-solid interactions with small scale in viscous fluid, the boundary layer affects the solution obviously, so no-slip boundary condition is needed. As for no-slip boundary, the viscous stress on the surface of solid boundary should be considered and the parameter  $\alpha$  can be calculated with Eq. (20) according to the kinematic viscosity coefficient  $\nu$  of the fluid. Since the local Reynolds number  $Re_h = Uh/\nu$  should not be larger than

$O(10)$ , for some viscous simulations with small kinematic viscosity coefficient  $\nu$ , the smoothing length  $h$  should be very small to satisfy the above criterion, i.e. we need very fine particle resolution. Sometimes one can use relatively coarse particle resolution by adding additional viscosity for the fluid, but on the interface between the solid boundary and the fluid, real kinematic viscosity coefficient  $\nu$  should be used for satisfying an accurate boundary condition. With the method above, one can achieve relatively accurate results for some weakly viscous cases with larger smoothing length, and computational cost is therefore saved a lot which is very necessary in practical applications of ocean engineering.

### 2.3. The motions of the solid body

As for the floating rigid body on the free surface, its velocity can be divided into two parts: translational velocity and rotational velocity. The conservation equations of momentum and moment of momentum of the solid body are as follows ([Oger et al., 2006](#)),

$$\begin{cases} \frac{D\mathbf{U}_c}{Dt} = \frac{\mathbf{F}_{\text{fluid-solid}}}{M} + \mathbf{g} \\ \frac{D\Omega_c}{Dt} = \frac{\mathbf{T}_{\text{fluid-solid}}}{I} \end{cases} \quad (21)$$

where  $M$ ,  $I$ ,  $\mathbf{U}_c$  and  $\Omega_c$  denote the mass of the body, the moment of inertia about the centroid  $c$ , the translational velocity and rotational velocity, respectively. Based on the momentum balance between the fluid and the rigid body particles, one can calculate the resultant force  $\mathbf{F}_{\text{fluid-solid}}$  and resultant moment  $\mathbf{T}_{\text{fluid-solid}}$  on the rigid body as follows:

$$\begin{cases} \mathbf{F}_{\text{fluid-solid}} = \sum_{i \in \text{fluid}} \sum_{j \in \text{solid}} -[(V_i^2 + V_j^2) \tilde{p}_{ij} + 2(d+2)\nu\rho_0\pi_{ij}V_iV_j] \nabla_i W_{ij} \\ \mathbf{T}_{\text{fluid-solid}} = \sum_{i \in \text{fluid}} \sum_{j \in \text{solid}} -\left(\frac{\mathbf{x}_i + \mathbf{x}_j}{2} - \mathbf{x}_c\right) \times [-(V_i^2 + V_j^2) \tilde{p}_{ij} + 2(d+2)\nu\rho_0\pi_{ij}V_iV_j] \nabla_i W_{ij} \end{cases} \quad (22)$$

Eq. (22) is similar to the force and torque derived in [Bouscasse et al. \(2013\)](#) in which the method of stress analysis is used. Here an improvement is made in the calculation of resultant moment  $\mathbf{T}_{\text{fluid-solid}}$  that  $(\mathbf{x}_i + \mathbf{x}_j)/2$  is used to denote the position of a point on the surface of the rigid body. Since in the present work, the surface of the rigid body is discretized into four layers of particles, see more details in [Section 2.4](#), most of the rigid particles are inside the surface of the body, directly using  $\mathbf{x}_j$  may make the calculation of resultant moment  $\mathbf{T}_{\text{fluid-solid}}$  too smaller. In addition, if free-slip boundary condition is implemented, the viscous terms in  $\mathbf{F}_{\text{fluid-solid}}$  and  $\mathbf{T}_{\text{fluid-solid}}$  should not be considered.

According to the principle of rigid body kinematics, the velocity and acceleration of the rigid body particles can be written as follows:

$$\begin{cases} \frac{D\mathbf{x}_j}{Dt} = \mathbf{u}_j \\ \mathbf{u}_j = \mathbf{U}_c + \Omega_c \times (\mathbf{x}_j - \mathbf{x}_c) \\ \mathbf{a}_j = \frac{D\mathbf{U}_c}{Dt} + \frac{D\Omega_c}{Dt} \times (\mathbf{x}_j - \mathbf{x}_c) + \Omega_c \times (\mathbf{u}_j - \mathbf{U}_c) \end{cases} \quad (23)$$

where subscript  $j$  denotes the rigid body particle. The velocity  $\mathbf{u}_j$  is used in the position updating of the rigid body particles. The acceleration  $\mathbf{a}_j$  will be used in the solid boundary implementation introduced in [Section 2.4](#). Besides, translational velocity  $\mathbf{U}_c$  and rotational velocity  $\Omega_c$  are updated in every time step according to Eq. (21). The explicit time integral method is introduced in [Section 2.5](#).

### 2.4. Boundary condition

In SPH method, the boundary implementation technology substantially determines the accuracy and stability of the final simulation results. Within the flow field, second order accuracy is obtained for kernel approximation ([Liu and Liu, 2003](#)), while at

near the boundary, because of the truncation of kernel function, approximation errors are introduced. Therefore, the boundary treatments have been cared a lot in literatures (Colagrossi et al., 2009; Liu et al., 2012; Maciá et al., 2011). In hydrodynamics, the boundary conditions can be classified into two types: (1) the free surface boundary condition; (2) the solid wall boundary condition.

On the free surface, the fluid flows must satisfy the kinematic condition and dynamic condition (Newman, 1977), as follows:

- (1) *Kinematic condition*: The fluid particles initially on the free surface will always remain on the free surface;
- (2) *Dynamic condition*: The free surface pressure is equal to the atmospheric pressure, usually set to be zero when the air effects and surface tension are not considered.

The free surface condition is addressed in detail by Colagrossi et al. (2009), and it is concluded that, due to the Lagrangian property, the kinematic condition can be satisfied naturally within WCPH framework, while for the dynamic condition, first order accuracy is obtained for inviscid flows. That is to say, as the smoothing length  $h$  approaching zero, the free surface condition in SPH can be satisfied implicitly without any special treatments.

As for the solid wall boundary (regardless of the solid wall boundary is stationary or moving), an impermeable boundary condition must be satisfied. In addition, for the flows of lower Reynolds number, a no-slip condition needs to be satisfied. Up to now, an optimal way to treat the solid wall boundary is to initially distribute dummy particles and an extrapolation technique is used to determine the detailed field values (pressure and velocity) of these dummy particles (Adami et al., 2012).

#### 2.4.1. Pressure extrapolation of dummy particles

It is shown in Fig. 1 that within the boundary wall, four layers of dummy particles are distributed since an improved Gaussian kernel function is used here. Note that, for 2-D problems, in order to make the solid boundary surface smooth, the four layers of dummy particles are distributed along four paralleled lines along and within the solid wall surface, and the distances between these paralleled lines are  $\Delta x$  which is the initial particle spacing of the fluid particles (for 3-D problems, the dummy particles are distributed on four layers of planes with the distance equal to  $\Delta x$ ). When a fluid particle approaches the solid wall, it enters the influence domain of a dummy particle, as shown in Fig. 1. In order to ensure the impermeable condition, the particle should not approach or leave along the center line direction between the fluid particle and the dummy particle (blue line connecting the fluid particle and the dummy particle in Fig. 1). Therefore, the

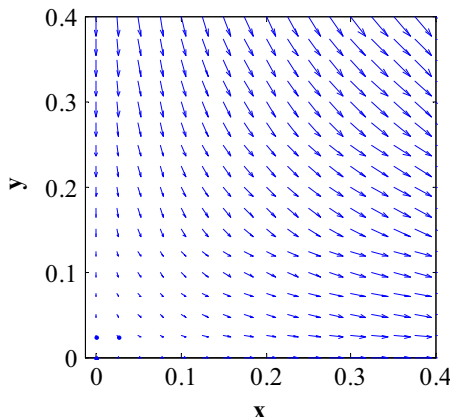


**Fig. 2.** The velocity field  $\mathbf{u} = (x, -y)$ ,  $(0 \leq x \leq 0.4, 0 \leq y \leq 0.4)$  for the divergence operator analysis.

acceleration of the fluid particle  $\mathbf{a}_f$  should be equal to the acceleration of the dummy particle  $\mathbf{a}_w$  in the center line direction as follows:

$$\mathbf{a}_w \cdot \frac{\mathbf{x}_{wf}}{|\mathbf{x}_{wf}|} = \mathbf{a}_f \cdot \frac{\mathbf{x}_{wf}}{|\mathbf{x}_{wf}|} \quad (24)$$

where subscript  $w$  refers to the dummy particle and subscript  $f$  refers to the fluid particle.  $\mathbf{x}_{wf} = \mathbf{x}_f - \mathbf{x}_w$  denotes the vector from the dummy particle  $\mathbf{x}_w$  to the fluid particle  $\mathbf{x}_f$  and  $|\mathbf{x}_{wf}|$  denotes the distance between them. Eq. (24) ensures the equal velocity along the center line between the two interacting particles in the next time step (since in the previous time step, it is assumed that the velocities are equal in the center direction). In Eq. (24),  $\mathbf{a}_f$  can be calculated from the momentum equation, as follows:

$$\mathbf{a}_f = \left( -\frac{\nabla p_f}{\rho_f} + \mathbf{g} + \frac{\mathbf{F}_V}{\rho_f} \right) \quad (25)$$

where the viscous stress  $\mathbf{F}_V$  is considered here, which is an improvement based on the dummy particle boundary proposed in Adami et al. (2012) since in some cases, viscous force may be considerable and the ignorance of  $\mathbf{F}_V$  may cause some boundary penetration. Substitute Eq. (25) into Eq. (24) and transpose, one gets

$$\nabla p_f \cdot \frac{\mathbf{x}_{wf}}{|\mathbf{x}_{wf}|} = (\rho_f \mathbf{g} + \mathbf{F}_V - \rho_f \mathbf{a}_w) \cdot \frac{\mathbf{x}_{wf}}{|\mathbf{x}_{wf}|} \quad (26)$$

where  $\nabla p_f \cdot (\mathbf{x}_{wf}/|\mathbf{x}_{wf}|)$  denotes the directional derivative of pressure at  $\mathbf{x}_f$  along the center line direction from  $\mathbf{x}_w$  to  $\mathbf{x}_f$ . According to the definition of directional derivatives,

$$\nabla p_f \cdot \frac{\mathbf{x}_{wf}}{|\mathbf{x}_{wf}|} = \frac{p_f - p_w}{|\mathbf{x}_{wf}|} \quad (27)$$

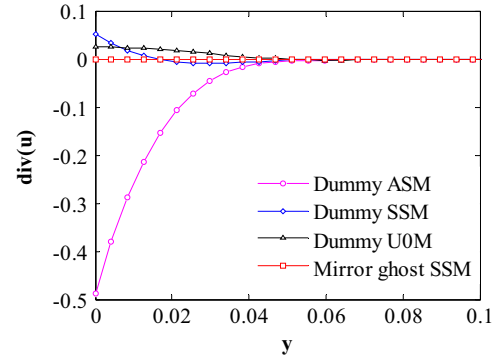


**Fig. 3.** Velocity divergence  $\text{div}(\mathbf{u})$  of  $\mathbf{u} = (x, -y)$ ,  $(x = 0.25, 0 \leq y \leq 0.1)$  with ASM, SSM, U0M extension, compared with mirroring ghost boundary.

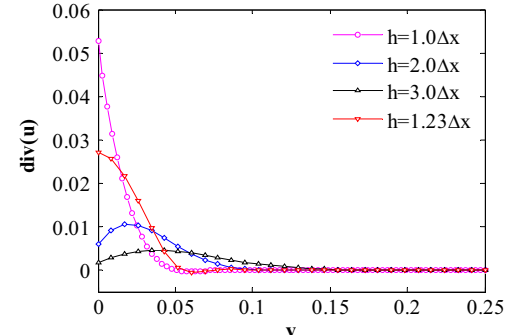


**Fig. 4.** Velocity divergence  $\text{div}(\mathbf{u})$  of  $\mathbf{u} = (x, -y)$ ,  $(x = 0.25, 0 \leq y \leq 0.25)$  computed with different smoothing length  $h$ .

Substituting Eq. (27) into Eq. (26), one obtains

$$p_w = p_f - (\rho_f \mathbf{g} + \mathbf{F}_V - \rho_f \mathbf{a}_w) \cdot \mathbf{x}_{wf} \quad (28)$$

Since one fluid particle usually interacts with several dummy boundary particles, as is shown in Fig. 1. Therefore, the interpolation method in Hu and Adams (2006) is used to calculate the final pressure of the dummy particles, as follows:

$$p_w = \frac{\sum_f p_f W_{wf} - \sum_f (\rho_f \mathbf{g} + \mathbf{F}_V - \rho_f \mathbf{a}_w) \cdot \mathbf{x}_{wf} W_{wf}}{\sum_f W_{wf}} \quad (29)$$

where subscript  $f$  refers to all the fluid particles in the supported domain of one dummy particle. After the pressure  $p_w$  of the dummy particle is calculated, substitute it into the equation of state, the density  $\rho_w$  of the dummy particle can be obtained,

$$\rho_w = \frac{p_w}{c_0^2} + \rho_0 \quad (30)$$

Note that, in the fixed ghost boundary technique (Marrone et al., 2011), the acceleration of the interpolation point and the ghost particle are equal along the normal direction of the solid wall surface, while in the present work, they are equal in the center line direction. This is because in the fixed ghost boundary, the pressure of ghost particle is calculated from only one certain interpolation point in the normal direction outside the solid wall, for more details, see in Marrone et al. (2011). While in the dummy particle boundary technique, the pressure of dummy particle is extrapolated from several fluid particles. From the opposite perspective, one fluid particle interacts with several dummy particles and the interacting forces between these particles pairs are all along the directions of their center lines, see in Fig. 1; therefore, the composition of these forces will be along the normal direction of the solid wall surface as the particle resolution increasing (when viscous stress is ignored). In this way, the generations of interpolation points are not needed, which makes the dummy particle technology easy to be conducted and suitable for ocean engineering applications.

Regarding the computational cost of the present boundary method, it is similar to the fixed ghost boundary in Marrone et al. (2011). Before the calculation of  $D\mathbf{u}/Dt$  for fluid particles, a previous subroutine which consists of a loop over all the particle pairs is needed for the pressure extrapolation and velocity extension (see in Section 2.4.2). This may increase the computational cost compared with some traditional boundary method, e.g. mirroring ghost boundary (Colagrossi and Landrini, 2003). However, the pressure extrapolation and velocity extension are only calculated between rigid and fluid particles. Moreover, with the particle resolution improving, the proportion of the rigid particle number in the total particle number will be smaller. Therefore, the increment of the computational cost due to the present boundary implementation is negligible.

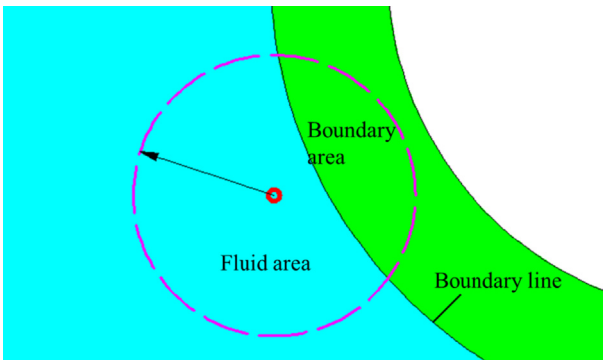


Fig. 5. Sketch of SPH approximation near the solid wall boundary.

#### 2.4.2. Velocity extension of dummy particles

As for the velocity extension, the method in Hu and Adams (2006) can be used as follows:

$$\mathbf{u}_{ext} = \frac{\sum_f \mathbf{u}_f W_{wf}}{\sum_f W_{wf}} \quad (31)$$

While  $\mathbf{u}_{ext}$  should not be assigned directly to the dummy particles. The velocity extension needs to be considered respectively for the velocity divergence approximation and viscous stress calculation.

**2.4.2.1. Velocity divergence approximation.** A theoretical analysis about the relationship between velocity divergence approximation and the dummy (ghost) particle velocity is made in De Leffe et al. (2011). It is concluded that the velocity divergence approximation is consistent and convergent if the dummy particle velocity component is equal to  $\mathbf{u}_{ext}$  in the tangential direction and equal to  $2\mathbf{u}_b - \mathbf{u}_{ext}$  in the normal direction of the solid boundary surface, where  $\mathbf{u}_b$  is the velocity of the solid boundary particle. This is also named as symmetric extension (SSM) in literatures (Maciá et al., 2011). In dummy particle boundary, this technique has been tested, which has been proved to cause serious penetration near the intersection between the free surface and the solid boundary. So in the present work, for the divergence approximation, the velocity of dummy particle is never extrapolated from the fluid particles, but use the local velocity according to the motions of the solid body (i.e. constant extension (UOM)), which was originally used in Adami et al. (2012).

When a no-slip boundary is implemented, the velocities of the dummy particles may be extrapolated equal to  $2\mathbf{u}_b - \mathbf{u}_{ext}$  in both the tangential and normal directions of the solid boundary surface (i.e. anti-symmetric extension (ASM), (Merino-Alonso et al., 2013)). While in this way, the velocity divergence approximation near the solid boundary has been proved to be inconsistent (Maciá et al., 2011). In this part, a test originally implemented by Colagrossi et al. (2009) to analyze the consistency of free surface and then used by Merino-Alonso et al. (2013) to analyze solid wall boundary condition is adopted to test the accuracy of the velocity divergence approximation near dummy particle boundary. It is assumed that the velocity field is  $\mathbf{u} = (x, -y)$ ,  $(0 \leq x \leq 0.4, 0 \leq y \leq 0.4)$ , as plotted in Fig. 2. In this test, the particle spacing is  $\Delta x = 0.025$  and the smoothing length is  $h = 1.23\Delta x$ . The dummy boundary particles are distributed below  $y = 0$ .

Three kinds of velocity extension are implemented for the dummy particles: constant extension (UOM), symmetric extension (SSM), and anti-symmetric extension (ASM). The classic mirroring ghost boundary (Colagrossi and Landrini, 2003) is used as a reference since the boundary line is straight. The velocity divergence approximation at  $x = 0.25$  is shown in Fig. 3. It can be seen that in dummy particle boundary, UOM extension is relatively better for the velocity divergence approximation, because the result is more close to zero, which is the analytic result. The result of SSM extension seems well, but it has been tested and serious penetration exists near the intersection between the free surface and the solid boundary. ASM extension gives a relatively worse result, so it is not used here. Besides, the mirroring ghost boundary can give a very accurate result, but it is only suitable for a

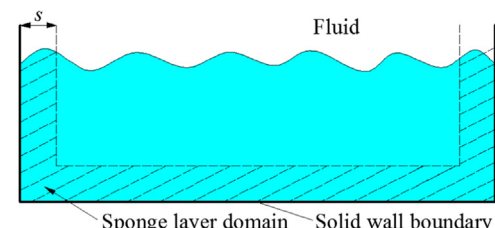


Fig. 6. Sketch of the sponge layer inside the solid wall boundary.

straight boundary. If the smoothing length  $h$  in the UOM extension is increased, the divergence approximation will converge to the analytic result, as shown in Fig. 4. This is because the discretization error decreases with the increasing number of interpolation particles.

After the numerical tests above, the accuracy of the velocity divergence approximation near the solid boundary is theoretically analyzed for UOM extension. In Fig. 5, when a fluid particle approaches the boundary line, the supported domain of the fluid particle is divided into two parts: the boundary area and the fluid area. In the boundary area, it is filled with dummy particles whose velocities are equal to the corresponding velocities in the solid body. Note that there is no kernel truncation here, so the velocity divergence approximation error in kernel approximation is only owing to the velocity extension in the boundary area. According to Section 2.1.1, one obtains

$$\langle \nabla \cdot \mathbf{u} \rangle = \int_{\Omega_f} \nabla \cdot \mathbf{u}_f W(\mathbf{x} - \mathbf{x}_f, h) d\mathbf{x}_f + \int_{\Omega_b} \nabla \cdot \mathbf{u}_b W(\mathbf{x} - \mathbf{x}_b, h) d\mathbf{x}_b \quad (32)$$

where  $\Omega_f$  and  $\Omega_b$  denote fluid area and boundary area in Fig. 5, respectively. According to Eq. (23), the second term on the right-hand side of Eq. (32) becomes

$$\int_{\Omega_b} \nabla \cdot \mathbf{u}_b W(\mathbf{x} - \mathbf{x}_b, h) d\mathbf{x}_b = \int_{\Omega_b} \nabla \cdot (\mathbf{U}_c + \Omega_c \times \mathbf{x}_{cb}) W(\mathbf{x} - \mathbf{x}_b, h) d\mathbf{x}_b \quad (33)$$

Take notice of that  $\mathbf{U}_c$  is a constant value, thus  $\nabla \cdot \mathbf{U}_c = 0$ , and

$$\begin{aligned} & \nabla \cdot (\mathbf{U}_c + \Omega_c \times \mathbf{x}_{cb}) \\ &= \nabla \cdot (\Omega_c \times \mathbf{x}_{cb}) \\ &= \mathbf{x}_{cb} \cdot (\nabla \times \Omega_c) - \Omega_c \cdot (\nabla \times \mathbf{x}_{cb}) \\ &= 0. \end{aligned} \quad (34)$$

So the velocity divergence approximation near the solid boundary is

$$\langle \nabla \cdot \mathbf{u} \rangle = \int_{\Omega_f} \nabla \cdot \mathbf{u}_f W(\mathbf{x} - \mathbf{x}_f, h) d\mathbf{x}_f \quad (35)$$

Since the fluid particles can only get near the boundary, and never overlap or penetrate the boundary line. As the smoothing length  $h$  approaching zero, one obtains

$$\begin{aligned} \langle \nabla \cdot \mathbf{u} \rangle &= \nabla \cdot \mathbf{u}_{\lim} \int_{\Omega_f} W(\mathbf{x} - \mathbf{x}_f, h) d\mathbf{x}_f \\ &= \nabla \cdot \mathbf{u} + O(h) \end{aligned} \quad (36)$$

Then the velocity divergence approximation converges to the accurate value with first order accuracy. Note that, the discretization error has not been considered in the present analysis. The

analysis above is similar to the discussion in Colagrossi et al. (2009) about the consistency of SPH approximation near the free surface. Besides, it is also pointed out in Colagrossi et al. (2011) that the local inconsistencies will not obviously affect the global quantities in the flow field. Moreover, in the present work, it has been proved in both 2-D and 3-D cases (see in Section 3) that there are neither penetrations nor instabilities near the solid boundary and the results agree well with experimental data and other numerical results.

**2.4.2.2. Viscous stress calculation.** As for the viscous stress near the solid boundary, it can be classified into two types according to different solid boundary conditions:

- 1) *Free-slip*: The viscous stress contributed by the dummy particle is never considered, and then free-slip boundary condition is satisfied (Adami et al., 2012).
- 2) *No-slip*: According to Bouscasse et al. (2013), no-slip boundary condition can be satisfied if the dummy particle velocity component is equal to  $\mathbf{u}_{ext}$  in the normal direction of the solid boundary surface and equal to  $2\mathbf{u}_b - \mathbf{u}_{ext}$  in the tangential direction.

In summary, the dummy particle velocity in viscous stress calculation is as follows,

$$\begin{cases} \mathbf{u}_f - \mathbf{u}_w = 0, & \text{free-slip} \\ \begin{cases} \mathbf{u}_w \cdot \mathbf{n}_s = \mathbf{u}_{ext} \cdot \mathbf{n}_s \\ \mathbf{u}_w \cdot \mathbf{t}_s = (2\mathbf{u}_b - \mathbf{u}_{ext}) \cdot \mathbf{t}_s \end{cases} & \text{no-slip} \end{cases} \quad (37)$$

where  $\mathbf{n}_s$  and  $\mathbf{t}_s$  denote the outside normal direction and the tangential direction on the solid boundary surface, respectively. The dummy particle boundary presented here is easy to be implemented in 3-D cases with complex boundary shapes. Therefore, it is suitable to be used in the applications of ocean engineering, where the concerned floating body shapes are usually irregular.

#### 2.4.3. Sponge layer

A sponge layer is implemented inside the stationary solid boundary wall with a thickness of  $s$  in order to reduce the non-physical pressure reflection, as is shown in Fig. 6. This sponge layer was originally used in Gong et al. (2009). For the fluid particles inside the sponge layer, Eqs. (15) and (16) should be multiplied with another term, as follows:

$$\left( \frac{D\rho_i}{Dt} \right)_{\text{sponge}} = \left( 1 - 100^{-0.9^{50s}} \right) \left( \frac{D\rho_i}{Dt} \right) \quad (38)$$

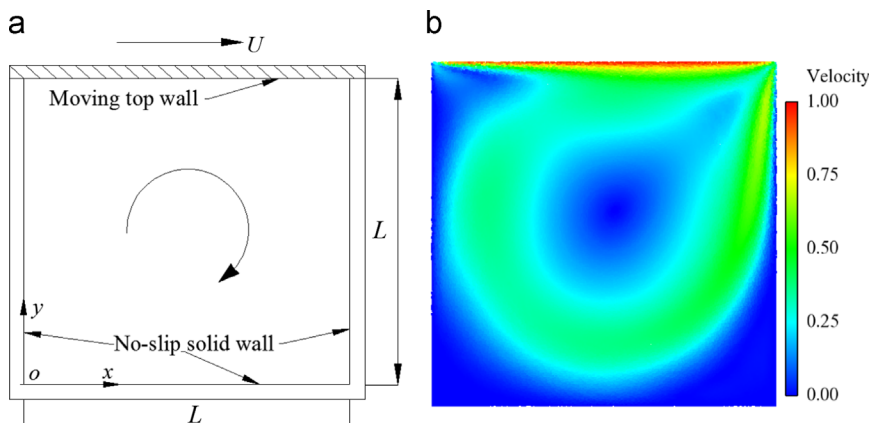
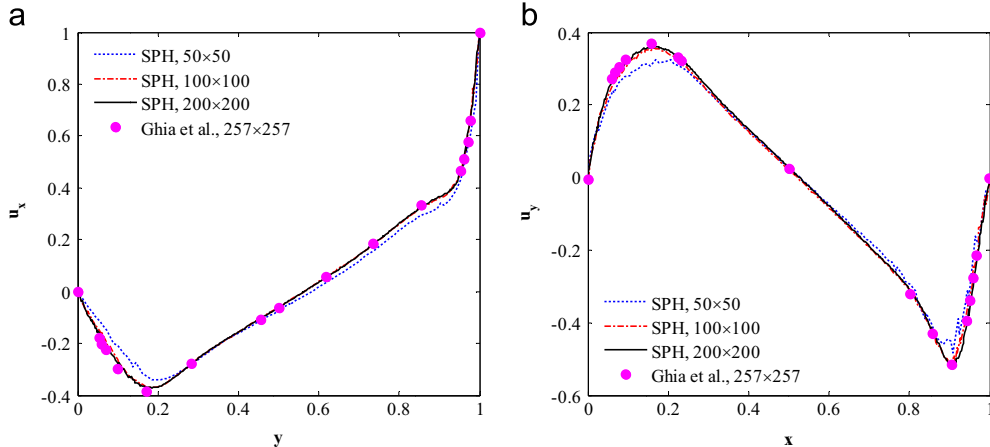
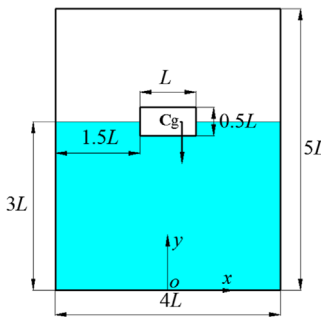


Fig. 7. (a) Sketch of the lid-driven cavity test; (b) contour of velocity in the rectangular cavity when the flow becomes steady at  $t = 40$ .



**Fig. 8.** Velocity profiles on  $x = 0.5$ (a) and  $y = 0.5$ (b).



**Fig. 9.** Sketch of the 2-D test case with an asymmetric mass distribution box.

$$\left(\frac{D\mathbf{u}_i}{Dt}\right)_{\text{sponge}} = \left(1 - 100^{-0.9^{50\lambda}}\right) \left(\frac{D\mathbf{u}_i}{Dt}\right) \quad (39)$$

where  $\lambda$  is defined as  $\lambda = d/s$ ,  $d$  is the perpendicular distance between the fluid particles  $i$  and the solid boundary wall.

### 2.5. Time step

Since WCPSPH is an explicit algorithm, the 4th order Runge-Kutta integration method is used in the present work. At each time step, four times searching of the nearest particle pairs are needed and therefore the simulation results are of high precision and good stability. Large amount of calculations seem to exist in this integration manner, while the time step  $\Delta t$  is permitted to be larger than the predictor-corrector scheme (Monaghan, 1994) or the Verlet scheme (Verlet, 1967). For the sake of simplicity, the changing rate of generic quantities like material position  $\mathbf{x}$ , velocity  $\mathbf{u}$ , density  $\rho$ , translational velocity  $\mathbf{U}_c$  and rotational velocity  $\Omega_c$  can be simplified as follows (Antuono et al., 2012):

$$\frac{D\mathbf{q}}{Dt} = \mathbf{F}(\mathbf{q}) \quad (40)$$

The 4th order Runge-Kutta integration process is as follows:

$$\begin{cases} \mathbf{q}^{(0)} = \mathbf{q}^n \\ \mathbf{q}^{(1)} = \mathbf{q}^{(0)} + \mathbf{F}(\mathbf{q}^{(0)})\Delta t/2 \\ \mathbf{q}^{(2)} = \mathbf{q}^{(0)} + \mathbf{F}(\mathbf{q}^{(1)})\Delta t/2 \\ \mathbf{q}^{(3)} = \mathbf{q}^{(0)} + \mathbf{F}(\mathbf{q}^{(2)})\Delta t \\ \mathbf{q}^{(4)} = \mathbf{q}^{(0)} + [\mathbf{F}(\mathbf{q}^{(0)}) + 2\mathbf{F}(\mathbf{q}^{(1)}) + 2\mathbf{F}(\mathbf{q}^{(2)}) + \mathbf{F}(\mathbf{q}^{(3)})]\Delta t/6 \\ \mathbf{q}^{n+1} = \mathbf{q}^{(4)} \end{cases} \quad (41)$$

where  $\mathbf{q}^{(1-4)}$  denotes the update of the field values in every searching of nearest particle pairs within each time step.  $\mathbf{q}^n$  denotes the generic quantities at the  $n$ th time step. In order to

keep the simulation accurate and stable, the magnitude of the time step  $\Delta t$  is restricted by three conditions below.

Account for the maximum acceleration of both the fluid and the solid body particles (Morris et al., 1997),

$$\Delta t \leq CFL_a \sqrt{\frac{h}{|\mathbf{a}|}}, |\mathbf{a}| = \max_i(|\mathbf{a}_f|, |\mathbf{a}_s|) \quad (42)$$

Considering the viscous-diffusion (Morris et al., 1997),

$$\Delta t \leq CFL_v \frac{h^2}{\nu} \quad (43)$$

Take the artificial sound speed into account (Monaghan and Kos, 1999),

$$\Delta t \leq CFL_c \min_i \left( \frac{h}{c_0 + h \max_j \pi_{ij}} \right) \quad (44)$$

In above,  $CFL_a = 0.25$ ,  $CFL_v = 0.125$ ,  $CFL_c = 2.0$  is adopted respectively, and the final time step  $\Delta t$  is chosen as the minimum of the above three values to ensure the stability.

### 3. Numerical tests

In this section, both 2-D cases and 3-D cases are applied to validate the present SPH model. In the 2-D cases, the first one is the well-known lid-driven cavity test which is challenging for SPH since it needs a stable viscous model and accurate boundary implementation. A rigid box rotating and sinking in viscous fluid is applied as the second test which is dedicated to verify the accuracy in the simulation of the interactions between the rigid body and the viscous fluid. After that, in order to test the ability of the boundary implementation in dealing with curved boundaries, 2-D cylinder water entry problem is selected as the third case and the results of SPH are compared with both experimental data and other numerical results. Engineers in ocean engineering are very concerned with the loading on the floating structures. Therefore, the fourth case is a wedge water entry problem. The pressure loading on the bottom of the wedge is measured and compared with experimental data in literatures.

A big advantage of the boundary implementation in Section 2.4 is the convenience in dealing with 3-D problems. Therefore, in 3-D cases, a 3-D dam breaking test is applied first to check the ability of the SPH model in approximating the pressure on a rigid obstacle. Then, 3-D cylinder entering undisturbed water with an initially oblique angle is simulated. This is a new model and the results of SPH are verified by our own experimental data.

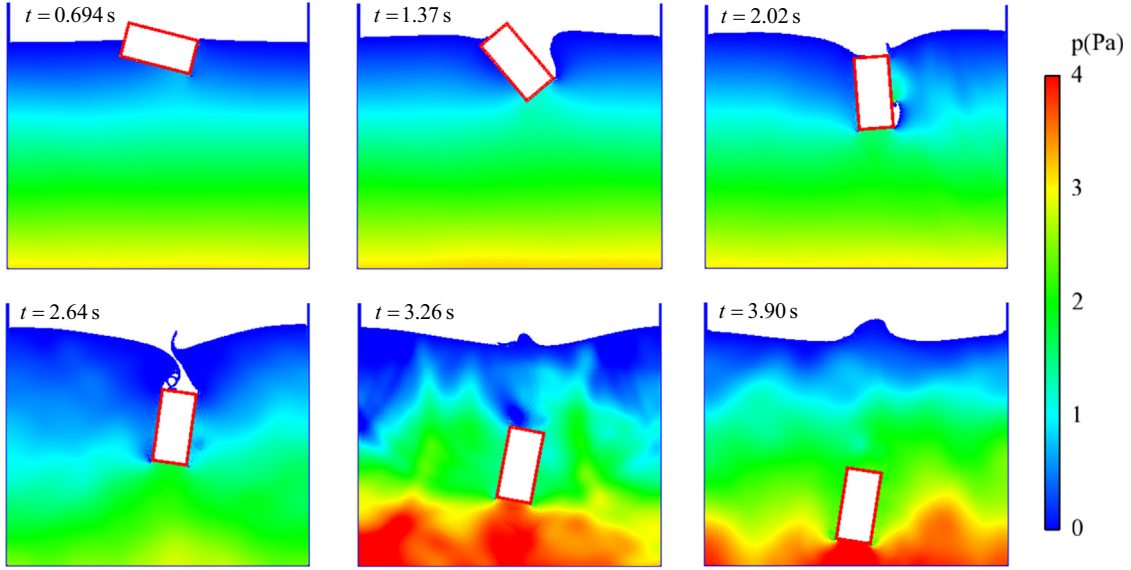


**Fig. 10.** Positions of the rigid body and the pressure field in the rectangular water tank at different time which increases left to right and top to bottom. The particle resolution is  $L/\Delta x = 100$ .

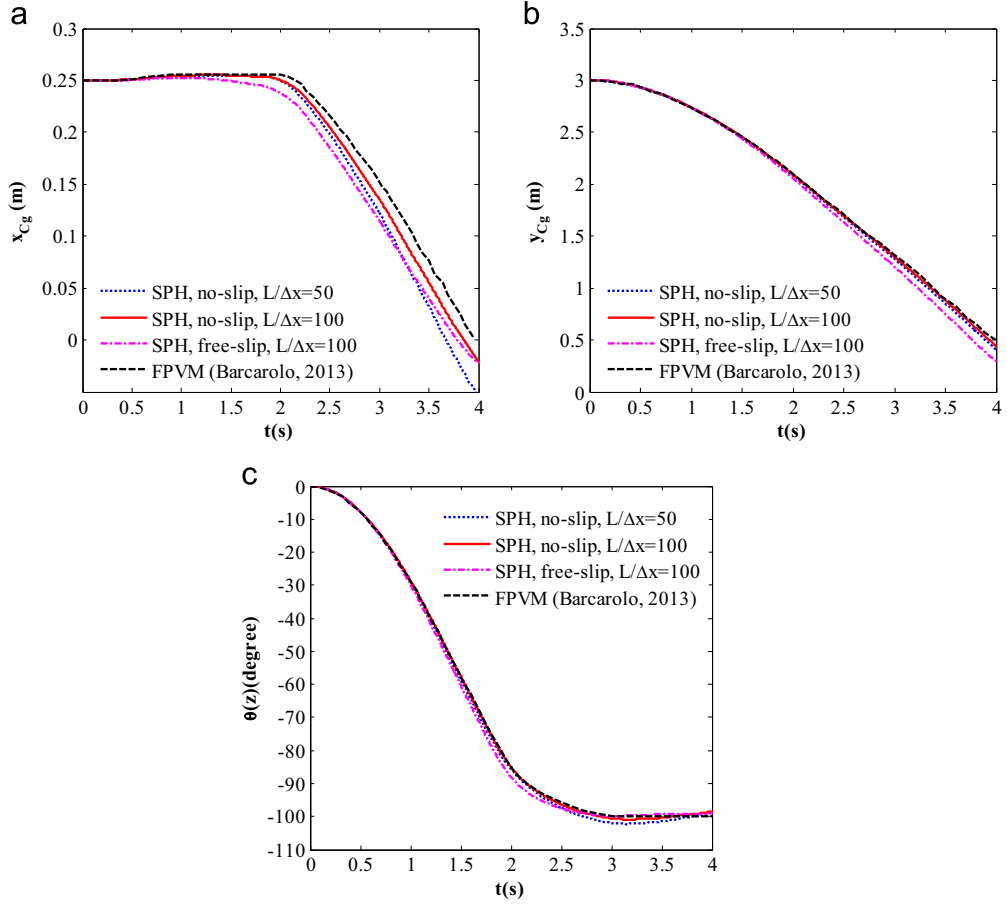


**Fig. 11.** The 3-DOF motions of the rigid box versus time compared with the results of FPVM in Barcarolo (2013).

### 3.1. 2-D cases

#### 3.1.1. Lid-driven cavity

The lid-driven cavity is applied here to test the viscous model. Besides, this case is also very effective in testing the accuracy of the no-slip solid wall boundary. Similar to the work by [Adami et al. \(2013\)](#), the results of [Ghia et al. \(1982\)](#) is used as the reference data

here. The sketch of the lid-driven cavity test is shown in [Fig. 7\(a\)](#). The length of the rectangular cavity is  $L = 1$ . All the boundaries in this test case are no-slip solid walls, where the top wall is moving with a constant velocity  $U = 1$ , while the other three sides are fixed. The initial density of the fluid inside the cavity is  $\rho_0 = 1$ . The Reynolds number here is  $Re = UL/\nu = 1000$ ; therefore,  $\nu = 0.001$ . The artificial sound speed is  $c_0 = 10U$ . The fluid domain in the

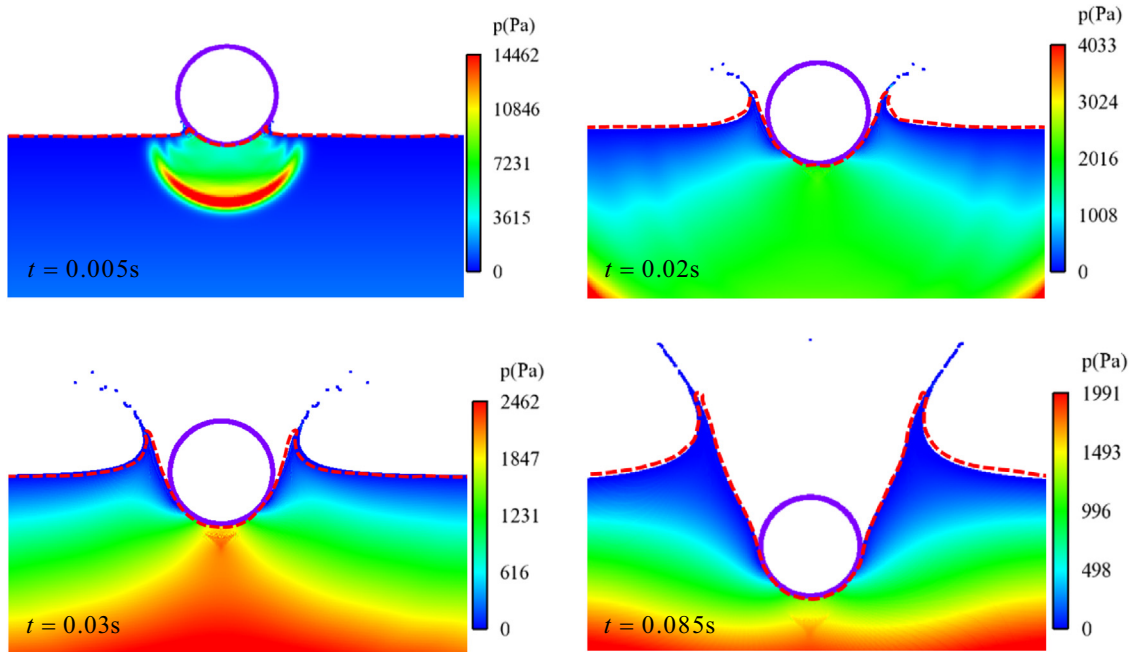


**Fig. 12.** The flow pattern and pressure contour of the 2-D cylinder water entry at  $t = 0.005$  s,  $t = 0.02$  s,  $t = 0.03$  s,  $t = 0.085$  s. The red dashed lines are the positions of free surface obtained by BEM in Sun and Faltinsen (2006). (For interpretation of the references to color in this figure legend, the reader is referred to the web version of this article.)

cavity is discretized by three particle resolutions which are  $50 \times 50$ ,  $100 \times 100$ ,  $200 \times 200$  in order to test the convergence of the viscous model. Note that, in order to prevent the flow voids caused by tensile instability (TI) which often happens in WSPH where the pressure field is very low, a background pressure  $p_b = 0.2$  is added in the equation of state in this case. The effects of  $p_b$  was analyzed in detail in Marrone et al. (2013) and Colagrossi et al. (2012).

When the summation of the kinetic energy of the fluid particles keeps a constant value in time, the flow system enters a steady state (Adami et al., 2013). In our model, at  $t = 40$ , the flow becomes steady, and the contour of velocity of the resolution  $200 \times 200$  is shown in Fig. 7(b). One may see clearly that a vortex forms in the middle of the rectangular cavity. Besides, the boundary layer near the solid wall is clear which shows the effectiveness of the no-slip boundary implementation. In order to give a quantitative validation,  $u_x$  at  $x = 0.5$  varying versus axis  $y$  and  $u_y$  at  $y = 0.5$  varying versus axis  $x$  are shown in Fig. 8. As the resolution increase from  $50 \times 50$  to  $100 \times 100$ , the velocity curve converge to the results of Ghia et al. (1982). The velocity curve of resolution  $100 \times 100$  and the one of resolution  $200 \times 200$  almost coincide, which shows a good convergence of the present viscous SPH model. The well agreements between the results of SPH and Ghia et al. (1982) also demonstrate that the solid wall boundary introduced in Section 2.4 is effective and accurate. The effectiveness of the viscous model establishes a good foundation for the simulation of interactions between rigid body and viscous fluid.

### 3.1.2. A rigid box rotating and sinking in viscous liquid

In this part, a rigid box rotating and sinking in viscous fluid is simulated. The sketch of the 2-D test case is shown in Fig. 9. The results of Finite Volume Particle Method (FVPM) in Barcarolo (2013) are used as reference data here since FVPM gives results with high accuracy even though its computational cost is expensive. The same to the case in Barcarolo (2013), the length of the rigid box is  $L = 1$  m. The gravity center  $C_g$  of the rigid box initially locates at (0.25 m, 3 m). The reference density of the fluid is

$\rho_0 = 1 \text{ kg/m}^3$  and the gravity acceleration is  $g = 1 \text{ m/s}^2$ . The mass and moment of inertia is  $M = 1 \text{ kg}$  and  $I = 0.083 \text{ kg m}^2$ , respectively. The kinematic viscosity coefficient of the fluid is  $\nu = 1/500 \text{ m}^2/\text{s}$ .

In the numerical test, the fluid domain is discretized into two particle resolutions,  $L/\Delta x = 50$  and  $L/\Delta x = 100$ , in order to test of the convergence of the SPH model. The artificial sound speed is  $c_0 = 10\sqrt{3gL}$ . The sponge layer in Section 2.4.3 is not used in this test since the rigid box is initially set to be stationary and no considerable non-physical pressure waves are radiated into the fluid. The motions of the rigid box are free in three degrees of freedom (3-DOF) after released. Both no-slip and free-slip boundary conditions are applied in this case to test the effects of viscous stress.

The position evolution of the rigid box and the contour of pressure in the fluid with the particle resolution of  $L/\Delta x = 100$  in no-slip boundary condition are shown in Fig. 10. One may notice that the pressure noise is reduced well. Due to its asymmetric mass distribution, the rigid box starts to rotate after released, see  $t = 0.694$  s and  $t = 1.37$  s in Fig. 10. In the meanwhile, since the rigid box is twice as heavy as the surrounding fluid, the box is sinking. At  $t = 2.02$  s, the free surface slams on the right top side of the box and big slamming force prevents the further rotation. At the same time, a cavity forms at the right side of the box in the fluid. At  $t = 2.64$  s, the free surface above the rigid box is nearly to hit each other and a cavity will form at the tail of the box. Since here a single phase SPH model is applied, the pressure inside the cavity is always zero. The cavity is closed at  $t = 3.26$  s. As time going on, from  $t = 3.26$  s to  $t = 3.90$  s, the rigid box sinks with an almost unchanged roll angle  $\theta(z)$ .

It can be observed in Fig. 10 that the hitting of the free surface and the closing of the cavity produce some non-physical pressure waves inside the flow domain, see for example at  $t = 3.26$  s. The existing of these non-physical pressure waves is a main drawback of WSPH, which is caused by the weakly compressible assumption. However, for the test in this part, the fluid-solid interaction is not so violent and the non-physical pressure waves produce little negative effects to the final results.

Time history curves of the 3-DOF motions on the gravity center of the rigid box are shown in Fig. 11. The results of SPH are

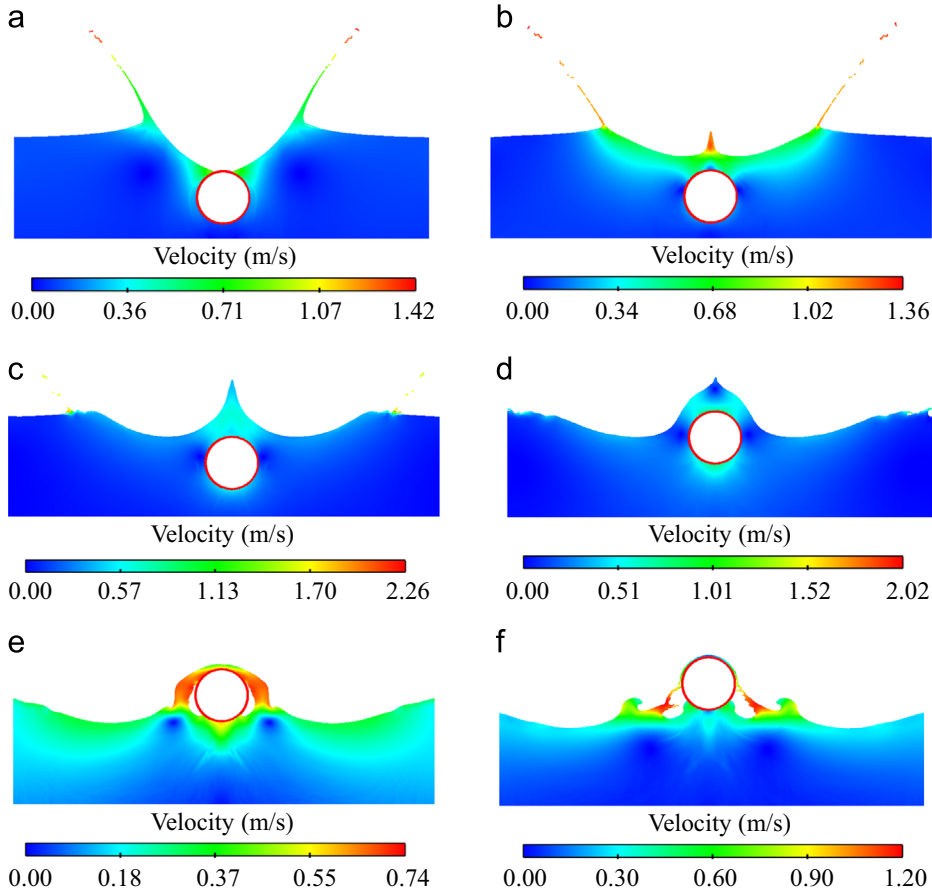


**Fig. 13.** The flow pattern and velocity contour of the cylinder water entry case at (a)  $t = 0.173$  s, (b)  $t = 0.252$  s, (c)  $t = 0.330$  s, (d)  $t = 0.405$  s, (e)  $t = 0.468$  s, (f)  $t = 0.568$  s.

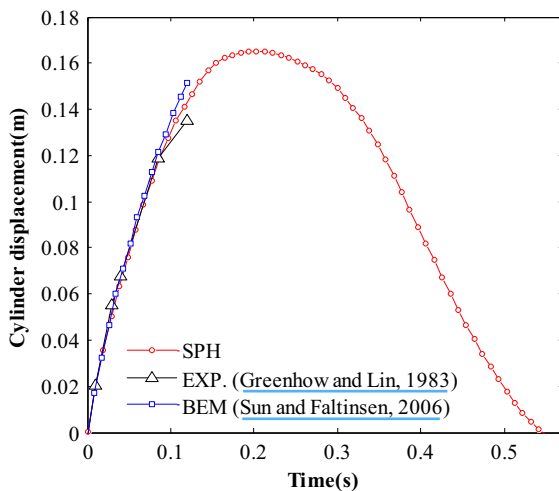


**Fig. 14.** The cylinder displacement versus time compared with the experimental data in Greenhow and Lin (1983) and BEM results in Sun and Faltinsen (2006).

compared with the results of FVPM (Barcarolo, 2013). The overall trends of these motions between SPH and FVPM agree well. It is observed that, for no-slip boundary conditions, as the particle resolution increasing, the results of SPH converge to the results of FVPM. However, since the viscous stress plays an important role in the motions of the rigid box, the results of free-slip boundary condition diverge a little from the reference data, especially in the time history of  $y_{Cg}$  in Fig. 11 that without viscous stress, the rigid box sinks faster. The reason is that, in no-slip cases, the viscous fluid acts considerable frictional forces on the rigid body, which

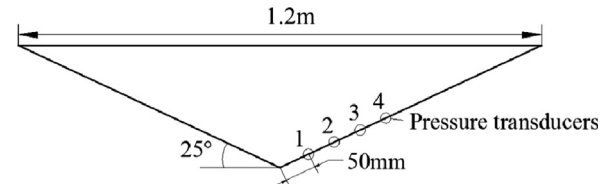


**Fig. 15.** Sketch of the wedge used in both the experiment (Yetto et al., 2006) and the present SPH simulation. Four pressure transducers are chosen where the impact pressure is measured.

decreases its sinking velocity. The difference between the results of free-slip and no-slip boundary conditions demonstrates that the viscous effects at the boundary should not be ignored. Therefore, we summarize as follows: on one hand, if real viscous stress is considered in the SPH model, we should apply an accurate no-slip boundary condition at the solid walls to achieve accurate results; on the other hand, if the viscous term in the governing equations is served as an artificial viscosity to stabilize the simulation, then free-slip boundary condition should be applied to avoid providing extra frictional forces.

### 3.1.3. Water entry of 2-D cylinder

Water entry of 2-D cylinder is simulated in this part and the SPH results are compared with the experimental data in Greenhow and Lin (1983). The cylinder with the diameter of  $d = 0.11$  m is dropped from the height of  $H_{drop} = 0.5$  m. The reference density of the fluid is  $\rho_0 = 1000 \text{ kg/m}^3$  and the gravity acceleration is  $g = 9.8 \text{ m/s}^2$ . The weight of the cylinder  $Mg$  is half of the buoyancy  $f_b$  when the cylinder is fully immersed.

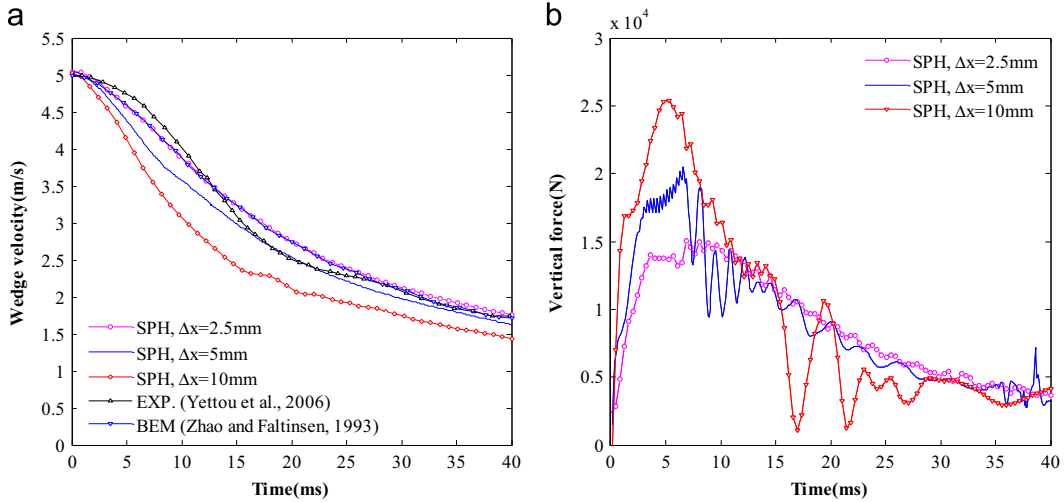


**Fig. 16.** (a) The falling velocity versus time compared with the experimental data in Yettou et al. (2006) and BEM results in Zhao and Faltinsen (1993); (b) the vertical force versus time.

In the SPH model, the cylinder falls down from touching the free surface with initial velocity  $u_0 = \sqrt{2g(H_{drop} - d/2)} = 2.955 \text{ m/s}$ . The water domain has a width of 1.0 m and a depth of 0.65 m, and the initial particle spacing is  $\Delta x = 0.001 \text{ m}$ . The artificial sound speed is  $c_0 = 25 \text{ m/s}$ . A free-slip boundary is implemented on the cylinder since the artificial viscous term in the equation of momentum is mainly for stabilizing the simulation. The sponge layer with the thickness of  $s = 0.05 \text{ m}$  is implemented inside the solid wall (see in Section 2.4.3) in order to reduce the pressure reflection.

The flow pattern and pressure contour after the cylinder entering water are shown in Fig. 12. The shapes of the free surface are compared with results of BEM (Sun and Faltinsen, 2006) and good agreements are obtained. Owing to the relatively fine particle resolution in our SPH model, splashing and fragment of the free surface are well reproduced. Regarding the pressure distribution in the fluid, one may notice that, at  $t = 0.005 \text{ s}$ , obvious pressure waves are radiated into the fluid. At  $t = 0.02 \text{ s}$ , the pressure waves have propagated further. Thanks to the sponge layer introduced in Section 2.4.3, the reflection of these non-physical pressure waves are prevented at near the solid wall boundary; therefore, one can see that at  $t = 0.03 \text{ s}$  and  $t = 0.085 \text{ s}$ , the contour of pressure is reasonable.

In the experiment of Greenhow and Lin (1983) and BEM simulation of Sun and Faltinsen (2006), the results for a period of only 0.12 s are presented. However, since the density of the cylinder is only half of the water, it will decelerate and rise up under the buoyancy force after it entering water. The whole motion process is simulated in this part with the present SPH method. The flow patterns after  $t = 0.12 \text{ s}$  which have seldom been presented in other literatures are shown in Fig. 13. The displacement-time curve of the cylinder is shown in Fig. 14, in which the SPH results are compared with those of experimental data (Greenhow and Lin, 1983) and BEM results (Sun and Faltinsen, 2006) until  $t = 0.12 \text{ s}$ . At  $t = 0.173 \text{ s}$  in Fig. 13, the free surface is nearly to close, which may cause some difficulties for the continuation of the simulation with BEM. As can be deduced in Fig. 14 that after  $t = 0.2 \text{ s}$ , the falling velocity of the cylinder is reduced to zero, and the cylinder begins to rise up. Then the simulation here is similar to the water exit of a horizontal cylinder simulated in Liu et al. (2014). The cylinder accelerates its rising due to the considerable buoyancy from  $t = 0.252 \text{ s}$  to  $t = 0.405 \text{ s}$  in Fig. 13. One may observe that there forms two flow voids at each side of the cylinder at  $t = 0.468 \text{ s}$  in Fig. 13. We analyze that, since the pressure on the free surface is always zero

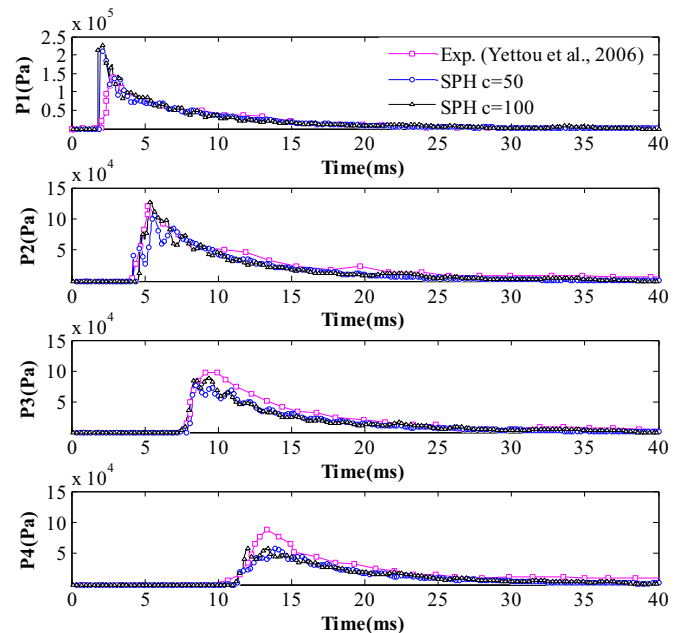


**Fig. 17.** The pressure-time curves compared with the experimental data in Yettou et al. (2006) at the pressure transducers from P1 to P4.

(Colagrossi et al., 2009), when the cylinder gets close to the free surface, the pressure field around the cylinder is decreasing and it may become negative in its downstream flow. Consequently, the tensile instability (TI) is possibly to happen, which would induce clumping of particles and eventually non-physical voids exist (Marrone et al., 2013). Unfortunately, in free surface flows, background pressure which is very effective to prevent non-physical voids cannot be added. In the future, similar to Gong et al. (2010), a multiphase SPH model may be adopted and background pressure can be added to prevent the existing of low-pressure area. But that relies on an excellent parallel computing since time step is restricted by the lighter phase in multiphase SPH model. Particle shifting technique proposed by Xu et al. (2009) and further improved by Lind et al. (2012) for free surface flows can ensure the particle distributing uniformly and therefore prevent the formation of flow voids. However, this technique has only been used in ISPH and its effects in WSPH are not very clear at this

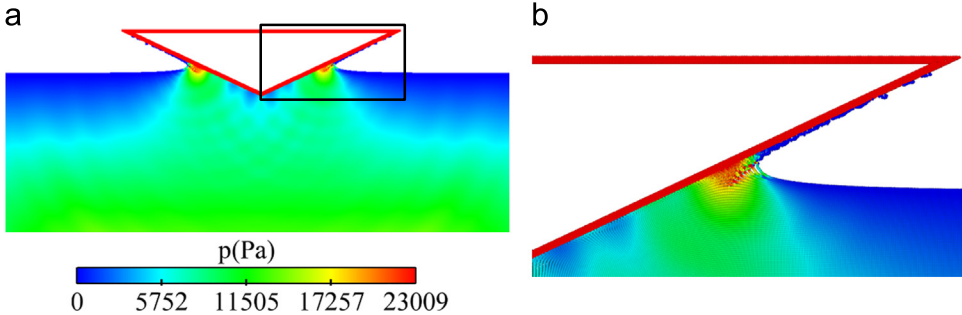


**Fig. 18.** (a) The pressures contour at  $t = 28$  ms after the wedge entering water; (b) the enlarged pressure contour in the black box in (a).

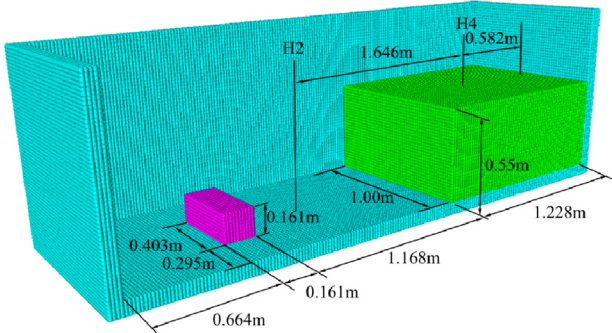


**Fig. 19.** The discretized SPH model of the 3-D dam breaking case.

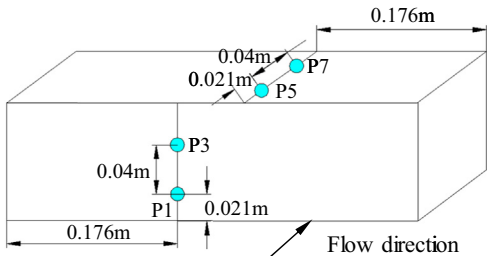


**Fig. 20.** Sketch of pressure transducers on the obstacle (P1, P3, P5, P7).

stage. Detailed researches about the prevention of TI are left for future works. Anyhow, in this part, it is shown that the boundary implementation is suitable for curved boundaries, the pressure inside the fluid is reasonable and the results of SPH agree well with experimental data and other numerical results.

### 3.1.4. Wedge water entry

When a ship or boat is sailing on the sea with an extremely high speed, due to the coupling effects of the ship and the induced waves, the bottom of the ship may rush out of the free surface, and then the bottom attacks on the free surface. A considerable pressure may load on the ship and even damage the ship structure. Calculations of these violent fluid-solid interactions are complex for the free surface which is largely deformed and broken. The ship bottom is usually simplified to be a 2-D wedge. In the traditional methods, like BEM ([Zhao and Faltinsen, 1993](#)), many assumptions are introduced. For example, the splashing fluid jet is assumed to be with less influence on the solutions and thus it is usually cut off. Besides, the fluid is assumed to be incompressible, non-viscous and irrotational. In this part, SPH method is used to simulate the wedge entry phenomenon which has also been numerically researched with ALE-SPH by [Koukouvinis et al. \(2013\)](#) and experimentally researched by [Yettou et al. \(2006\)](#). The results in this part are

compared with the experimental results in [Yettou et al. \(2006\)](#) and BEM results in [Zhao and Faltinsen \(1993\)](#) in order to validate the accuracy and stability of the present SPH scheme.

The sketch of the wedge is shown in Fig. 15. The deadrise angle of the wedge is  $\theta = 25^\circ$ , and the width of the top section of the wedge is 1.2 m. The mass of the wedge is  $M = 94$  kg. In the SPH model, the width and depth of the water domain is  $W = 2.5$  m and  $D = 1.1$  m, respectively. Wedge is dropped just from touching the free surface with an initial velocity of  $v_0 = \sqrt{2gH} = 5.05$  m/s according to the freely falling height with  $H = 1.3$  m in the experiment ([Yettou et al., 2006](#)). In order to test the convergence of the present SPH scheme, three particle resolutions are used in this part,  $\Delta x = 2.5$  mm,  $\Delta x = 5$  mm and  $\Delta x = 10$  mm. The artificial sound speed  $c_0$  is 50 m/s. The wedge falling velocity and the vertical force versus time are measured, as shown in Fig. 16. As the particle resolution increases, the velocity attenuation becomes more slowly and the vertical force time curves become smoother. In Fig. 16(a), it is shown that the falling velocity of the wedge agrees well with BEM results ([Zhao and Faltinsen, 1993](#)) in the resolution of  $\Delta x = 2.5$  mm, and both the two numerical results show a little difference compared with the experimental data. This is because it is not an absolutely 2-D flow around the wedge in the experiment of [Yettou et al. \(2006\)](#) due to the finite length of the wedge.

In ocean engineering applications, the pressure loading on the floating structure is more concerned to the designers. Therefore, based on the relatively better particle resolution  $\Delta x = 2.5$  mm, the pressure loadings on the four chosen pressure transducers in Fig. 15 is measured with  $p_s = \sum_f p_f W_{sf} / \sum_f W_{sf}$  where the subscript  $f$  and  $s$  denote fluid particles and solid wall particles, respectively. Two artificial sound speed  $c_0 = 50$  m/s and  $c_0 = 100$  m/s are tested, and the pressure-time curves are shown in Fig. 17, which are compared with the experimental data in [Yettou et al. \(2006\)](#). From the pressure-time curves, the differences caused by the two artificial sound speeds are very little, which demonstrates that the effects of compressibility of the fluid are negligible. The pressure-time curves agree well with the experimental data except for the maximum pressure which is slightly smaller in SPH at the transducer 3 and 4. The diminution of the maximum pressure has also been mentioned in [Koukouvinis et al. \(2013\)](#). The global pressure quantities agree well with the experimental data and prove that the present SPH method is suitable for engineering applications.

Fig. 18(a) shows the pressure contour at  $t = 28$  ms after the wedge entering water, and the enlarged pressure contour around the bottom of the right side of the wedge is shown in Fig. 18(b). The largest pressure exists at the intersection between the free surface and the wedge bottom and that should be cared in ocean engineering designs. Since the deadrise angle of the wedge in this case is small ( $\theta = 25^\circ$ ), the pressure on the bottom of the wedge decreases from the area near free surface to the deadrise angle, which coincides with the experimental data in [Yettou et al. \(2006\)](#). However, one may find that, around the deadrise angle in Fig. 18, there are some pressure oscillations. A reason is that there are some non-physical pressure

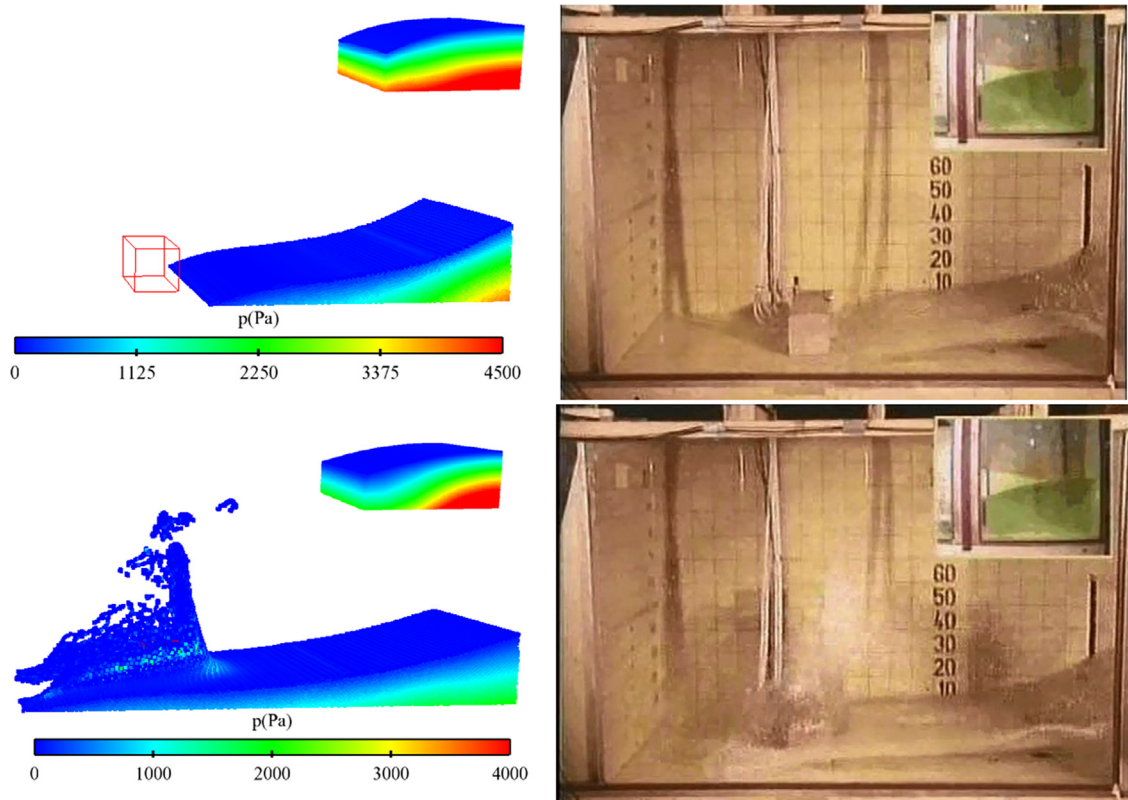


**Fig. 21.** Snapshots of the 3-D dam breaking test compared with experiment (Kleefsman et al., 2005) at  $t = 0.04$  s (top) and  $t = 0.056$  s (bottom). The snapshots of the experiment are cut out from the experimental video on the website of SPHERIC.

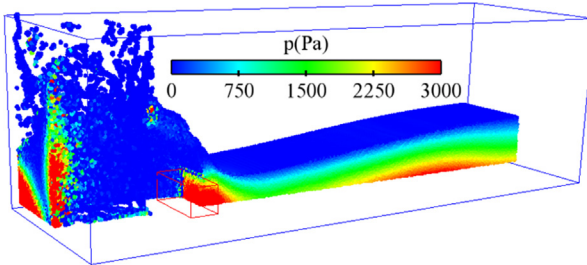


**Fig. 22.** Contour of pressure at  $t = 0.985$  s, only half of the flow domain is shown.

waves radiated from the high-pressure area near the free surface and they interfere with each other at around the deadrise angle. These non-physical pressure waves are caused by the weakly compressibility assumption in WCSph and they are also observed in the results of Gong et al. (2009). Besides, the pressure of the splashing fluid jet is nearly null, see in Fig. 18(b), therefore, the cut off in the BEM method in Zhao and Faltinsen (1993) is reasonable.

### 3.2. 3-D cases

#### 3.2.1. 3-D dam breaking

The 3-D dam breaking experiment was originally performed in Maritime Research Institute Netherlands to evaluate the green water loading on the deck equipment. It is a violent interaction between free surface and rigid body, which has been simulated by VOF method (Kleefsman et al., 2005), ISPH method (Lee et al., 2010), WCSph method (Lee et al., 2010) and MPS method (Khayyer and Gotoh, 2012). The 3-D dam breaking case is a very useful test for the validation of numerical schemes. WCSph method has been proved to perform worse in evaluating the pressure loading on the

rigid body surface (Lee et al., 2010). Here it is adopted to test the performance of the present SPH scheme.

The discretized SPH model of the 3-D dam breaking case and its geometric values are shown in Fig. 19. The locations of the pressure transducers on the obstacle are illustrated in Fig. 20, where two points P1, P3 are on the right side of the obstacle and two points P5, P7 on the topside. The initial particle spacing is  $\Delta x = 1.83$  mm, and free-slip boundary condition is assigned to the solid wall boundary. The artificial sound speed is  $c_0 = 25$  m/s. Snapshots of the 3-D dam breaking test compared with experiment (Kleefsman et al., 2005) at  $t = 0.4$  s and  $t = 0.56$  s are shown in Fig. 21 and good agreements are achieved on the shape and arrival time of the flow front. In order to see the local pressure details more clearly, contour of pressure at  $t = 0.985$  s is shown in Fig. 22. Since the flow is symmetric about the central plane, only half of the flow domain is shown. The flow front is first separated by the obstacle, and then impacts on the side wall, therefore high pressure areas form on the obstacle and in the corner of the side wall. After that, direction of flow is turned to the central. The impact of the flows from the two sides causes another high-pressure area in the middle. Eventually, a backward jet forms towards the obstacle.

In Fig. 23, the pressure-time curves at P1, P3, P5 and P7 simulated with the present SPH method are compared with the experimental data (Kleefsman et al., 2005). The pressures-time curves at P1 and P3 agree well with the experimental data, while at P5 and P7, some oscillations occur at around  $t = 1.0$  s. Especially at P5, during  $t = 0.5 – 1.2$  s in Fig. 10(c), there is a great pressure oscillation before the pressure climbs. This is because the pressure is measured with  $p_s = \sum_f p_f W_{sf} / \sum_f W_{sf}$ , which has reckoned the pressure at the right side of the obstacle (for the radius of the supported domain is  $3h$ , which has covered the right side of the obstacle). If improving the particle resolution, the pressure oscillation will be released. The water height at position H2 and H4 in

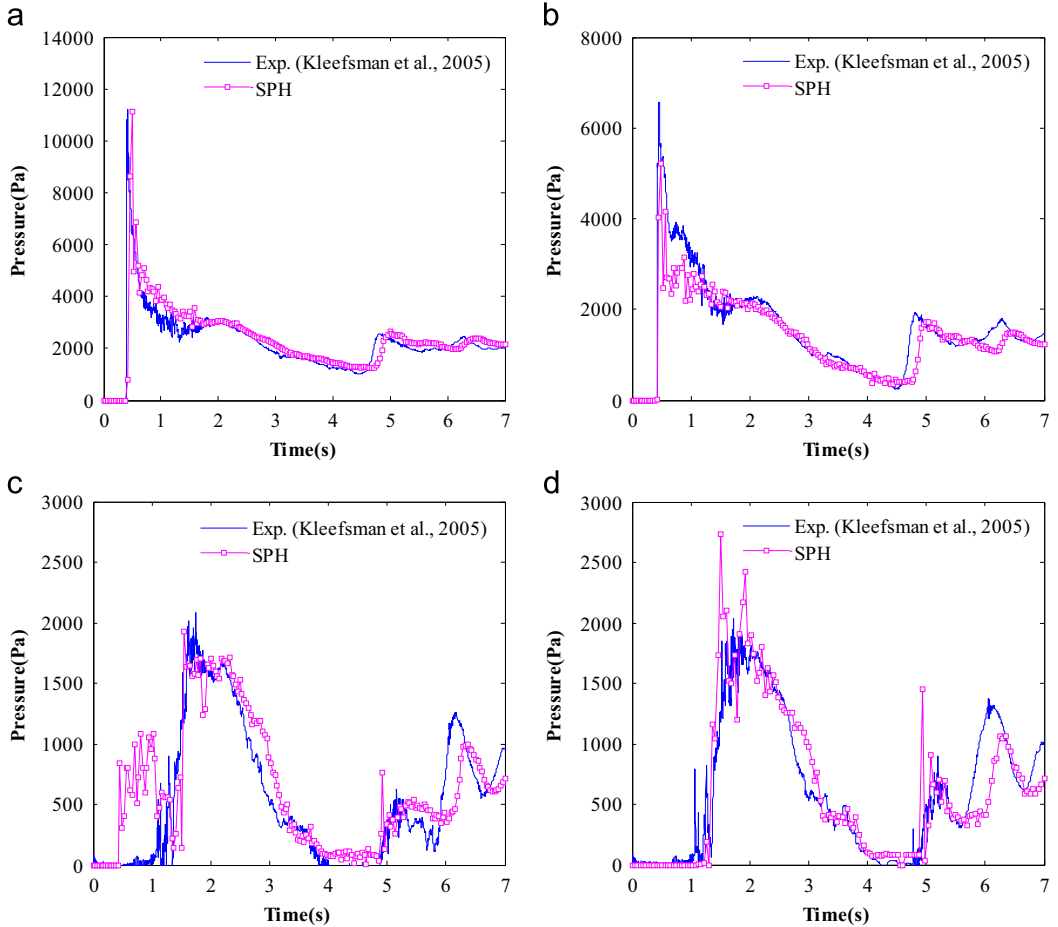


**Fig. 23.** Pressure-time curves at P1(a), P3(b), P5(c), P7(d), respectively, compared with experimental data in Kleefsman et al. (2005).

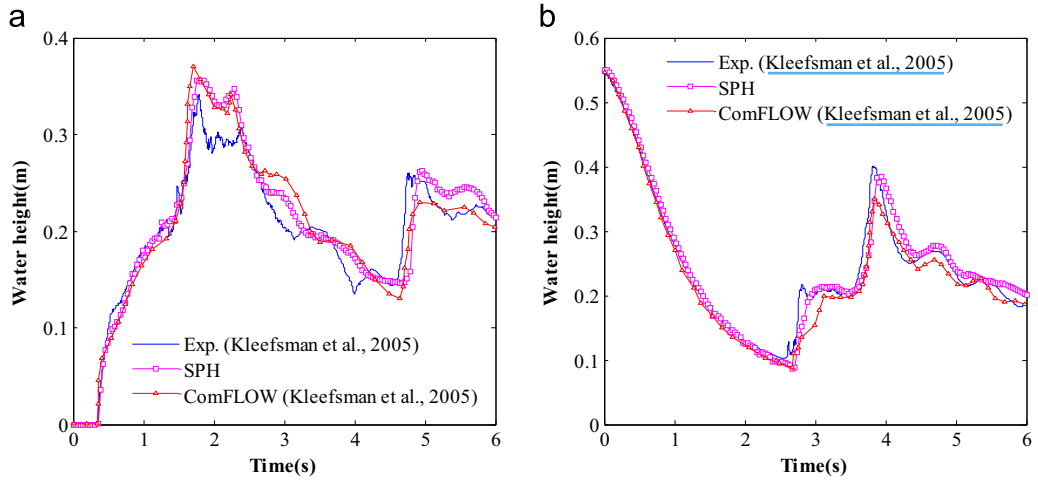


**Fig. 24.** The water height-time history compared with the results of ComFLOW and experimental data in Kleefsman et al. (2005) at vertical wave probe H2 (a) and H4 (b).

**Fig. 19** is measured in the SPH scheme. The SPH results are compared with the results of experiment and ComFLOW in Kleefsman et al. (2005) as plotted in Fig. 24, where a good agreement is achieved. Comparing Fig. 24(a) and (b), one may find that the SPH results on probe H4 are much better than those on probe H2. This is because the variation of water levels on probe H2 is much more complex than that on probe H4 and the particle resolution in our numerical test is not very fine. Besides, it is

observed that on probe H2, at  $t = 2$  s, the results of SPH agree well with the results of ComFLOW and the two numerical results both diverge a little from the experimental data. The reason is that, at the vicinity of the rigid obstacle (e.g. on probe H2), the flow structure is more complex, and the water levels there may be even different between two times of experiment (Lobovský et al., 2014).

The simulation results prove that the SPH scheme in the present work is robust and stable enough to simulate violent

interactions between free surface and stationary rigid body in three dimensions. Besides, the construction of the initial SPH model is so easy that it is suitable for the applications in ocean engineering practice, e.g. to evaluate the green water loading on the deck equipment.

### 3.2.2. Water entry of a 3-D cylinder

In this part, water entry of a cylinder with an oblique angle is experimentally measured using high speed camera and numerically simulated by SPH. The sketch of this case is shown in Fig. 25. The oblique angle  $\theta$  is  $35^\circ$ . The cylinder vertically enters the undisturbed pure water with an initial velocity of  $1.92 \text{ m/s}$ . Since the main purpose in this part is to verify the SPH method, series of experiments with variable oblique angles are not given. The cylinder is made of homogeneous plexiglass with the length of  $0.15 \text{ m}$  and the diameter of  $0.032 \text{ m}$ . The mass of the cylinder is  $M = 0.145 \text{ kg}$ . The whole entrance process of the cylinder is recorded by the Phantom V12.1 high-speed camera, and the time evolution of positions of the cylinder is measured with attached software toolkits.

In numerical test, the geometry model of the cylinder is constructed by the pre-process toolkit in the software Abaqus. The model consists of four layers of shells with the distance equal to initial particle spacing  $\Delta x = 2.4 \times 10^{-3} \text{ m}$  and each layer of the shell is meshed with quadrilateral grids, so the model can be read conveniently by our SPH solver. In the SPH model, the gravity center  $C_g$  of the cylinder locates at  $(-0.025 \text{ m}, 0.34 \text{ m})$ , see in Fig. 25. The length  $L$ , width  $W$  and height  $H$  of the fluid are

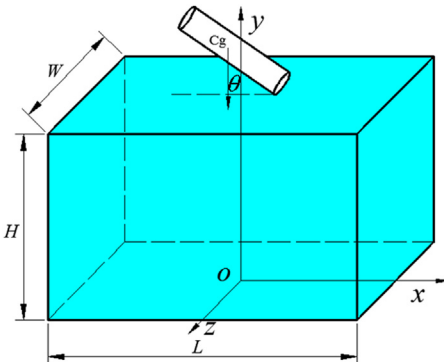


**Fig. 25.** Sketch of the 3-D cylinder water entry case.

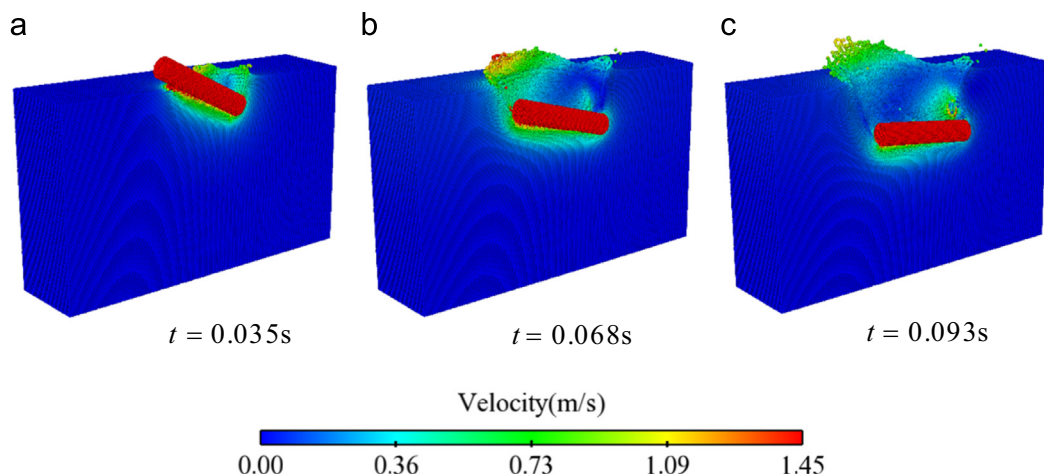


**Fig. 26.** Snapshots and contours of velocity at (a)  $t = 0.035 \text{ s}$ , (b)  $t = 0.068 \text{ s}$  and (c)  $t = 0.093 \text{ s}$ . Half of the fluid domain at one side of the coordinate plane  $oxy(z < 0)$  is shown.

discretized into 200, 100, 120 particles, respectively. There are totally about 2.724 million particles in this test. The fluid domain is large enough that the boundary effects to the motions of the cylinder are negligible. The artificial sound speed is  $c_0 = 20 \text{ m/s}$ . On the cylinder, free-slip boundary condition is implemented.

Snapshots and contour of velocity at  $t = 0.035 \text{ s}$ ,  $t = 0.068 \text{ s}$  and  $t = 0.093 \text{ s}$  are shown in Fig. 26. In order to show the flow patterns more clearly, half of the fluid domain at one side of coordinate plane  $oxy(z < 0)$  is shown since the flow is symmetric about this plane. It is observed in Fig. 26 that, as the cylinder penetrating the water surface, the cylinder is rotating toward horizontal and moving forward. This is caused by the initially oblique angle of the cylinder which induces asymmetrical hydrodynamic forces. Besides, the water splashing is also reproduced well. A jet is splashed first when the right side of the cylinder impacts on the water surface and then considerable water fragments are splashed up after left side of the cylinder entering water. Snapshots of experiment and SPH at  $t = 0.068 \text{ s}$  are shown in Fig. 27(a and b). One may find that the positions of the cylinder in experiment and SPH agree well. In Fig. 27(b), contour of pressure in SPH at  $t = 0.068 \text{ s}$  is also shown which demonstrates that the pressure noise is reduced effectively in 3-D fluid-solid interactions.

Time evolutions of the motions on the gravity center of the cylinder are compared between the experiment and SPH in Fig. 28, from which we may find that the overall trends of these motions agree well. The discrepancy between the horizontal motions is within about one particle size. The vertical motions between experiment and SPH are almost coincide before  $t = 0.068 \text{ s}$ . After  $t = 0.068 \text{ s}$ , the cylinder in the experiment falls a little more fast. Regarding the rotating angle  $\theta$ , the cylinder rotates faster in SPH. We analyze that, first, the particle resolution here is not very fine, which may cause some numerical errors. Second, the surface tension force and the cavity effect are not considered in SPH. We find that, surface tension force restricts the development of the gas cavity in the experiment, i.e. in the experiment, most part of the cylinder is surrounded by water, and gas cavity only exists at two ends of the cylinder, see in Fig. 27(a). While at the same time in SPH, the flow void above the cylinder is larger. Therefore, the drag force and the rotate moment in SPH are a little larger than those in the experiment, which makes the cylinder fall slower and rotate faster (since magnitude of the drag force and rotate moment is mainly determined by the pressure difference on the top and the bottom). In the future, with better particle resolution on the high-performance computer, a multiphase SPH model (Gong et al.,

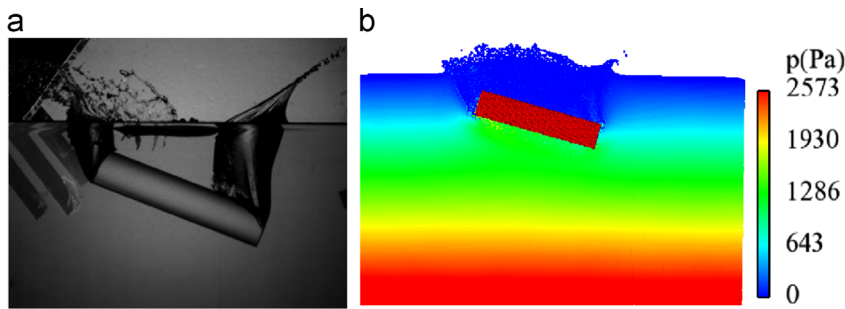


Fig. 27. Snapshot of the experiment (a) and contour of pressure by SPH (b), both are at  $t = 0.068$  s.

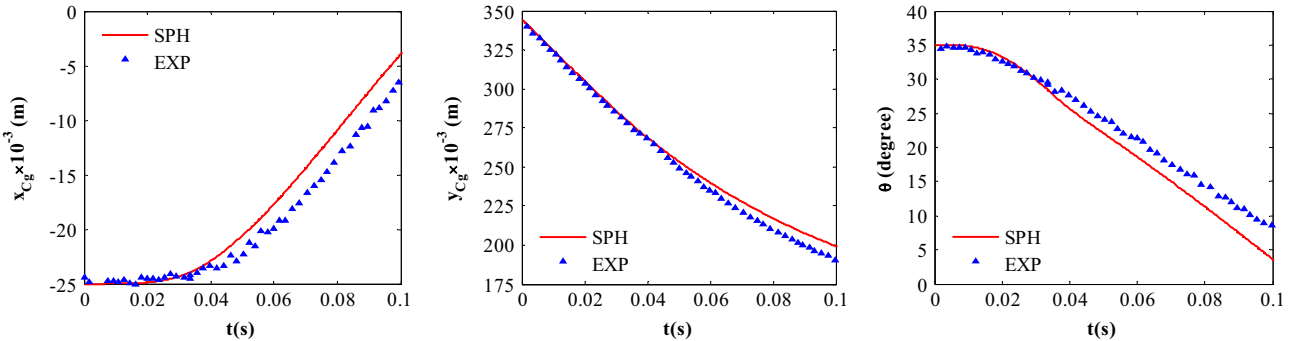


Fig. 28. Time evolutions of the motions of the cylinder. Results of SPH are compared with experimental data.

2010) considering surface tension force and cavity effects may be developed based on the present SPH model.

In conclusion, the motions of the cylinder in SPH globally agree with the results of experiment, and the shapes of the free surface are also similar. Besides, the pressure field in SPH is stable. The cylinder water entry case in this part demonstrates that the present SPH method is capable of simulating complex interactions between free surface and moving rigid body in three dimensions.

#### 4. Conclusions

A robust SPH scheme is applied to simulate violent interactions between free surface and rigid body. With the use of an improved Gaussian kernel, the artificial density diffusion, the artificial viscosity, the linearized state equation, the improved dummy particle boundary, and the 4th order Runge–Kutta integration method, the present SPH scheme is stable and accurate.

Some numerical techniques are improved in this paper. The forces and torques on the rigid body are improved for higher accuracy. The pressure of the dummy particle is derived in detail with the consideration of viscous stress. The accuracy of velocity divergence approximation near dummy particle boundary is analyzed. The extensions of dummy particle velocity for both the free-slip and no-slip solid boundary are presented.

Both 2-D cases and 3-D cases are introduced to test the present SPH scheme. We compare the results of SPH with either experimental data or other numerical results, and good agreements are achieved which demonstrate that the WCSph method in this paper can give acceptable results in the simulation of complex interactions between free surface and rigid body in both 2-D and 3-D problems.

In conclusion, the present SPH method is robust. But several problems still need to be solved, for example, the multi-spatial resolution is not used here, which has caused a large computational cost even though the scheme here is paralleled by OpenMp with eight threads in an Inter(R) Core(TM) i7-3770 processor. The multi-spatial resolution research is ongoing. The prevention of

tensile instability (TI) in free surface flows is still a challenging problem which needs attention.

#### Acknowledgements

The authors are very willing to appreciate the help of Andrea Colagrossi and Salvatore Marrone from CNR-INSEAN for their zealous and generous guidance and instructions. The authors would like to highly appreciate Dr. Huang Xiao, who made the expression in this paper well understood. Great appreciation is also given to Sun Chao, who helped us in the experiment.

This work is also supported by National Program for Support of Top-notch Young Professionals, the Excellent Young Scientists Fund of China (51222904) and the Lloyd's Register Foundation (LRF), a UK registered charity and sole shareholder of Lloyd's Register Group Ltd, which invests in science, engineering and technology for public benefit worldwide.

#### Appendix A. Supporting information

Supplementary data associated with this article can be found in the online version at <http://dx.doi.org/10.1016/j.oceaneng.2015.01.019>.

#### References

- Adami, S., Hu, X.Y., Adams, N.A., 2012. A generalized wall boundary condition for smoothed particle hydrodynamics. *J. Comput. Phys.* 231 (21), 7057–7075.
- Adami, S., Hu, X.Y., Adams, N.A., 2013. A transport-velocity formulation for smoothed particle hydrodynamics. *J. Comput. Phys.* 241 (0), 292–307.
- Antuono, M., Colagrossi, A., Marrone, S., 2012. Numerical diffusive terms in weakly-compressible SPH schemes. *Comput. Phys. Commun.* 183 (12), 2570–2580.
- Antuono, M., Colagrossi, A., Marrone, S., Molteni, D., 2010. Free-surface flows solved by means of SPH schemes with numerical diffusive terms. *Comput. Phys. Commun.* 181 (3), 532–549.
- Barcarolo, D.A., 2013. Improvement of the Precision and the Efficiency of the SPH Method: Theoretical and Numerical Study. Ph.D. Thesis. of Ecole Centrale de Nantes.

- Bouscasse, B., Colagrossi, A., Marrone, S., Antuono, M., 2013. Nonlinear water wave interaction with floating bodies in SPH. *J. Fluids Struct.* 42, 112–129.
- Buchner, B., 2002. Green Water on Ship-type Offshore Structures. Ph.D. Thesis.
- Chung, T., 2010. Computational Fluid Dynamics. Cambridge University Press.
- Colagrossi, A., Antuono, M., Le Touzé, D., 2009. Theoretical considerations on the free-surface role in the smoothed-particle-hydrodynamics model. *Phys. Rev. E* 79 (5), 056701.
- Colagrossi, A., Antuono, M., Souto-Iglesias, A., Le Touzé, D., 2011. Theoretical analysis and numerical verification of the consistency of viscous smoothed-particle-hydrodynamics formulations in simulating free-surface flows. *Phys. Rev. E* 84 (2), 026705.
- Colagrossi, A., Bouscasse, B., Antuono, M., Marrone, S., 2012. Particle packing algorithm for SPH schemes. *Comput. Phys. Commun.* 183 (8), 1641–1653.
- Colagrossi, A., Landri, M., 2003. Numerical simulation of interfacial flows by smoothed particle hydrodynamics. *J. Comput. Phys.* 191 (2), 448–475.
- De Leffe, M., Le Touzé, D., Alessandrini, B., 2009. Normal flux method at the boundary for SPH. In: Proc. SPHERIC, Fourth International Workshop, Nantes, France.
- De Leffe, M., Le Touzé, D., Alessandrini, B., 2011. A modified no-slip condition in weakly-compressible SPH. In: Proc. SPHERIC, Sixth International Workshop, Hamburg, Germany.
- Dehnen, W., Aly, H., 2012. Improving convergence in smoothed particle hydrodynamics simulations without pairing instability. *Mon. Not. R. Astron. Soc.* 425 (2), 1068–1082.
- Faltinsen, O.M., 1993. Sea Loads on Ships and Offshore Structures. Cambridge University Press.
- Faltinsen, O.M., 1977. Numerical solution of transient nonlinear free-surface motion outside or inside moving bodies. In: Proceedings Second Int. Conf. on Num. Ship Hydrodynamics, UC Berkeley, pp. 257–266.
- Faltinsen, O.M., Timokha, A.N., 2009. Sloshing. Cambridge University Press.
- Ghia, U., Ghia, K.N., Shin, C.T., 1982. High-Re solutions for incompressible flow using the Navier-Stokes equations and a multigrid method. *J. Comput. Phys.* 48 (3), 387–411.
- Gingold, R.A., Monaghan, J.J., 1977. Smoothed particle hydrodynamics theory and application to non-spherical stars. *Mon. Not. R. Astron. Soc.* 181, 375–389.
- Gong, K., Liu, H., Wang, B.I., 2009. Water entry of a wedge based on SPH model with an improved boundary treatment. *J. Hydraul. Ser. B* 21 (6), 750–757.
- Gong, K., Wang, B.I., Li, H., 2010. Modelling water entry of a wedge by multiphase sph method. In: Proceedings of 32nd Conference on Coastal Engineering, Shanghai, China.
- Greenhow, M., Lin, W.M., 1983. Nonlinear-free Surface Effects: Experiments and Theory, DTIC Document.
- Grenier, N., Antuono, M., Colagrossi, A., Le Touzé, D., Alessandrini, B., 2009. An hamiltonian interface SPH formulation for multi-fluid and free surface flows. *J. Comput. Phys.* 228 (22), 8380–8393.
- Hongbin, J., Xin, D., 2005. On criterions for smoothed particle hydrodynamics kernels in stable field. *J. Comput. Phys.* 202 (2), 699–709.
- Hu, X.Y., Adams, N., 2006. A multi-phase SPH method for macroscopic and mesoscopic flows. *J. Comput. Phys.* 213 (2), 844–861.
- Hu, X.Y., Adams, N., 2007. An incompressible multi-phase SPH method. *J. Comput. Phys.* 227 (1), 264–278.
- Khayyer, A., Gotoh, H., 2012. A 3D higher order laplacian model for enhancement and stabilization of pressure calculation in 3D MPS-based simulations. *Appl. Ocean Res.* 37, 120–126.
- Kleefsman, K., Fekken, G., Veldman, A., Iwanowski, B., Buchner, B., 2005. A volume-of-fluid based simulation method for wave impact problems. *J. Comput. Phys.* 206 (1), 363–393.
- Koshizuka, S., Oka, Y., 1996. Moving-particle semi-implicit method for fragmentation of incompressible fluid. *Nucl. Sci. Eng.* 123 (3), 421–434.
- Koukouvinis, P.K., Anagnostopoulos, I.S., Papantonis, D.E., 2013. Simulation of 2D wedge impacts on water using the SPH-ALE method. *Acta Mech.* 224 (11), 2559–2575.
- Landri, M., Colagrossi, A., Faltinsen, O., 2003. Sloshing in 2D flows by the SPH method. In: Eighth Int. Conf. on Num. Ship Hydrodynamics, Busan, Korea, pp. 1–15.
- Lee, E.S., et al., 2008. Comparisons of weakly compressible and truly incompressible algorithms for the SPH mesh free particle method. *J. Comput. Phys.* 227 (18), 8417–8436.
- Lee, E.S., Violeau, D., Issa, R., Ploix, S., 2010. Application of weakly compressible and truly incompressible SPH to 3-D water collapse in waterworks. *J. Hydraul. Res.* 48 (S1), 50–60.
- Lighthill, J., 1986. Fundamentals concerning wave loading on offshore structures. *J. Fluid Mech.* 173, 667–681.
- Lind, S.J., Xu, R., Stansby, P.K., Rogers, B.D., 2012. Incompressible smoothed particle hydrodynamics for free-surface flows: a generalised diffusion-based algorithm for stability and validations for impulsive flows and propagating waves. *J. Comput. Phys.* 231 (4), 1499–1523.
- Liu, G.R., Liu, M.B., 2003. Smoothed Particle Hydrodynamics: A Meshfree Particle Method. World Scientific.
- Liu, M.B., Liu, G.R., 2010. Smoothed particle hydrodynamics (SPH): an overview and recent developments. *Arch. Comput. Meth. E* 17 (1), 25–76.
- Liu, M.B., Shao, J.R., Chang, J.Z., 2012. On the treatment of solid boundary in smoothed particle hydrodynamics. *Sci. China Technol. Sci.* 55 (1), 244–254.
- Liu, M.B., Shao, J.R., Li, H.Q., 2014. An SPH model for free surface flows with moving rigid objects. *Int. J. Numer. Methods Fluids* 74, 684–697.
- Lobovský, L., Botía-Vera, E., Castellana, F., Mas-Soler, J., Souto-Iglesias, A., 2014. Experimental investigation of dynamic pressure loads during dam break. *J. Fluids Struct.* 48 (0), 407–434.
- Maciá, F., Antuono, M., González, L.M., Colagrossi, A., 2011. Theoretical analysis of the no-slip boundary condition enforcement in SPH methods. *Prog. Theory Phys.* 125 (6), 1091–1121.
- Marrone, S., 2012. Enhanced SPH Modeling of Free-surface Flows with Large Deformations (Ph.D. Thesis). University of Rome La Sapienza.
- Marrone, S., et al., 2011. δ-SPH model for simulating violent impact flows. *Comput. Methods Appl. Mech. Eng.* 200 (13), 1526–1542.
- Marrone, S., Colagrossi, A., Antuono, M., Colicchio, G., Graziani, G., 2013. An accurate SPH modeling of viscous flows around bodies at low and moderate Reynolds numbers. *J. Comput. Phys.* 245, 456–475.
- Merino-Alonso, P., Macia, F., Souto-Iglesias, A., Colagrossi, A., 2013. Consistency analysis of flow field extension models into ghost fluid regions for SPH solid body boundary condition implementations. In: Proc. SPHERIC, Eighth International Workshop, Trondheim, Norway.
- Molteni, D., Colagrossi, A., 2009. A simple procedure to improve the pressure evaluation in hydrodynamic context using the SPH. *Comput. Phys. Commun.* 180 (6), 861–872.
- Monaghan, J.J., Gingold, R., 1983. Shock simulation by the particle method SPH. *J. Comput. Phys.* 52 (2), 374–389.
- Monaghan, J.J., Kajtar, J., 2009. SPH particle boundary forces for arbitrary boundaries. *Comput. Phys. Commun.* 180 (10), 1811–1820.
- Monaghan, J.J., Kos, A., 1999. Solitary waves on a cretan beach. *J. Waterw. Port Coastal—ASCE* 125 (3), 145–155.
- Monaghan, J.J., 1994. Simulating free surface flows with SPH. *J. Comput. Phys.* 110 (2), 399–406.
- Monaghan, J.J., 2005. Smoothed particle hydrodynamics. *Rep. Prog. Phys.* 68 (8), 1703.
- Morris, J.P., Fox, P.J., Zhu, Y., 1997. Modeling low reynolds number incompressible flows using sph. *J. Comput. Phys.* 136 (1), 214–226.
- Newman, J.N., 1977. Marine Hydrodynamics. MIT Press.
- Oger, G., Doring, M., Alessandrini, B., Ferrant, P., 2006. Two-dimensional SPH simulations of wedge water entries. *J. Comput. Phys.* 213 (2), 803–822.
- Sibilla, S., 2007. SPH simulation of local scour processes. In: Proc. SPHERIC, Second International Workshop, Universidad Politécnica de Madrid, Spain.
- Skillicorn, A., Lind, S., Stansby, P.K., Rogers, B.D., 2013. Incompressible smoothed particle hydrodynamics (SPH) with reduced temporal noise and generalised fission smoothing applied to body-water slam and efficient wave-body interaction. *Comput. Methods Appl. Mech. Eng.* 265, 163–173.
- St-Germain, P., Nistor, I., Townsend, R., 2012. Numerical modeling of tsunami-induced hydrodynamic forces on onshore structures using SPH. *Coastal Eng. Proc.* 1 (33), 81.
- Sun, H., Faltinsen, O.M., 2006. Water impact of horizontal circular cylinders and cylindrical shells. *Appl. Ocean Res.* 28 (5), 299–311.
- Sun, S.L., Wu, G.X., 2013. Oblique water entry of a cone by a fully three-dimensional nonlinear method. *J. Fluids Struct.* 42, 313–332.
- Vandamme, J., Zou, Q., Reeve, D.E., 2011. Modeling floating object entry and exit using smoothed particle hydrodynamics. *J. Waterw. Port Coastal—ASCE* 137 (5), 213–224.
- Verlet, L., 1967. Computer "experiments" on classical fluids. I. Thermodynamical properties of lennard-jones molecules. *Phys. Rev.* 159 (1), 98.
- Wang, P., Yao, Y., Tulin, M.P., 1995. An efficient numerical tank for non-linear water waves, based on the multi-subdomain approach with BEM. *Int. J. Numer. Methods Fluids* 20 (12), 1315–1336.
- Wu, G.X., Ma, Q.W., Eatock Taylor, R., 1998. Numerical simulation of sloshing waves in a 3D tank based on a finite element method. *Appl. Ocean Res.* 20 (6), 337–355.
- Xu, R., Stansby, P., Laurence, D., 2009. Accuracy and stability in incompressible SPH (ISPH) based on the projection method and a new approach. *J. Comput. Phys.* 228 (18), 6703–6725.
- Yettou, E.M., Desrochers, A., Champoux, Y., 2006. Experimental study on the water impact of a symmetrical wedge. *Fluid Dyn. Res.* 38 (1), 47–66.
- Zhang, A.M., Cao, X.Y., Ming, F.R., Zhang, Z.F., 2013. Investigation on a damaged ship model sinking into water based on three dimensional SPH method. *Appl. Ocean Res.* 42, 24–31.
- Zhao, R., Faltinsen, O.M., 1993. Water entry of two-dimensional bodies. *J. Fluid Mech.* 246 (1), 593–612.
- Zheng, X., Duan, W.Y., Ma, Q.W., 2012. A new scheme for identifying free surface particles in improved SPH. *Sci. China Phys. Mech. Astron.* 55 (8), 1454–1463.